

Copyright © 2005 IEEE. Reprinted from

T. Makkonen, A. Holappa, J. Ellä, and M. M. Salomaa, “Finite element simulations of thin-film composite BAW resonators”, IEEE Transactions on Ultrasonics, Ferroelectrics, and Frequency Control, Vol. 48, No. 5, pp. 1241–1258, September 2001.

This material is posted here with permission of the IEEE. Such permission of the IEEE does not in any way imply IEEE endorsement of any of Helsinki University of Technology's products or services. Internal or personal use of this material is permitted. However, permission to reprint/republish this material for advertising or promotional purposes or for creating new collective works for resale or redistribution must be obtained from the IEEE by writing to pubs-permissions@ieee.org.

By choosing to view this document, you agree to all provisions of the copyright laws protecting it.

Finite Element Simulations of Thin-Film Composite BAW Resonators

Tapani Makkonen, *Member, IEEE*, Antti Holappa, Juha Ellä, and Martti M. Salomaa

(Invited Paper)

Abstract—A finite element method (FEM) formulation is presented for the numerical solution of the electroelastic equations that govern the linear forced vibrations of piezoelectric media. A harmonic time dependence is assumed. Both of the approaches, that of solving the field problem (harmonic analysis) and that of solving the corresponding eigenvalue problem (modal analysis), are described.

A FEM software package has been created from scratch. Important aspects central to the efficient implementation of FEM are explained, such as memory management and solving the generalized piezoelectric eigenvalue problem. Algorithms for reducing the required computer memory through optimization of the matrix profile, as well as Lanczos algorithm for the solution of the eigenvalue problem are linked into the software from external numerical libraries.

Our FEM software is applied to detailed numerical modeling of thin-film bulk acoustic wave (BAW) composite resonators. Comparison of results from 2D and full 3D simulations of a resonator are presented. In particular, 3D simulations are used to investigate the effect of the top electrode shape on the resonator electrical response. The validity of the modeling technique is demonstrated by comparing the simulated and measured displacement profiles at several frequencies. The results show that useful information on the performance of the thin-film resonators can be obtained even with relatively coarse meshes and, consequently, moderate computational resources.

I. INTRODUCTION

ACCURATE modeling of piezoelectric devices requires, in general, the application of numerical methods. This is due to the complexity of the piezoelectric equations that describe the device and its loading conditions, rendering analytical solutions of the equations for nontrivial 2D and 3D geometries exceedingly difficult. A general purpose, computer-aided numerical method for predicting the behavior of a physical system in response to external loads is the FEM [1]–[3]. The method is well established and has been widely used in numerous engineering disciplines. The general FEM formulation for linear piezoelectric materials was elaborated by Allik and Hughes [4]. Since then, FEM has been extensively applied in the simulation of piezoelectric devices, such as ultrasonic transducers [5], [6], surface acoustic wave (SAW) devices [7], [8], Lamb wave delay lines [9], and BAW resonators [10]. In this paper, we employ FEM in simulations of thin-film BAW resonators.

Manuscript received May 18, 2000; accepted April 18, 2001. This research is funded by Nokia Mobile Phones Ltd, Salo, Finland.

T. Makkonen, A. Holappa, and M. M. Salomaa are with the Materials Physics Laboratory, Helsinki University of Technology, FIN-02015 HUT, Finland (e-mail: tapani@focus.hut.fi).

J. Ellä is with Nokia Mobile Phones Ltd., FIN-24101 Salo, Finland.

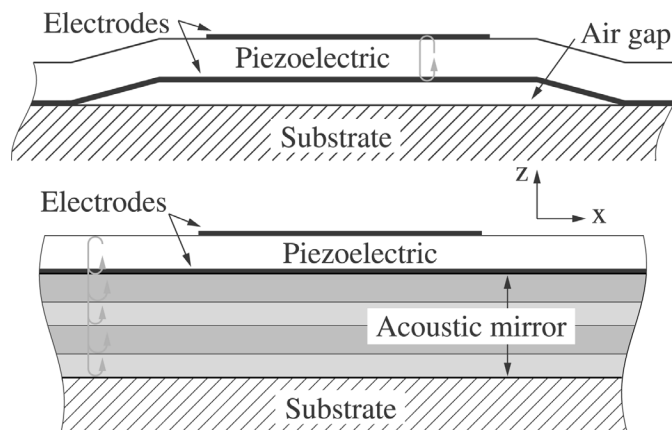


Fig. 1. Air gap and SMR composite thin-film BAW resonator configurations. In an air-gap resonator, the structure is suspended from both sides; in SMR, the resonator is fabricated atop an acoustic mirror, which prohibits wave penetration into the substrate.

Commercial, general purpose FEM software is often not well suited to the analysis of piezoelectric devices; the selection of elements and analysis types are commonly too limited. Therefore, a customized FEM software has been implemented, with matrix storage schemes and solution algorithms chosen, keeping in mind the particular requirements posed by the modeling of thin-film BAW resonators.

Thin-film BAW technology promises small-size resonators and filters with GHz-range operating frequencies, which are integrable with active RF circuits [11]–[13]. The composite resonators considered in this paper are membrane and solidly mounted resonator (SMR) configurations, shown in Fig. 1. In membrane resonators, the acoustic cavity is formed as the wave reflects from the air interfaces above and below the resonator. The early membrane-type composite BAW resonators [14], [15] were fabricated by etching from the backside of the substrate, which limits the number of components that can fit on the wafer. This problem was solved by the air-gap type resonators, where the air interface is formed by using either a sacrificial layer [11] or etching the substrate below the resonator [16]—both methods avoid the need for backside etching. Recently, SMR configurations have emerged, where quarter-wavelength thick layers—possessing alternately high and low acoustical impedances—acoustically isolate the resonator from the substrate [17].

The main challenge in the design of thin-film resonators is the suppression of side resonances that can be excited around the frequency of the desired mode, e.g., the funda-

mental longitudinal thickness mode. The spurious mode content depends on the geometry of the device, such as the thickness-to-width ratio. For large thickness-to-width ratios, 1D modeling [18]–[21] is considered to be adequate. For modeling in 2D, the mode-matching technique [22], [23], the finite difference frequency domain method [24], [25], and the FEM [26], [27] have been employed. 2D models are considered to be adequate for configurations with narrow and long electrodes [28], such as monolithic crystal filters (MCF). However, the electrode dimensions dictated by electrical matching often are such that accurate results do not warrant 1D or 2D modeling. Therefore, we have studied the spurious resonances through full 3D FEM simulations.

Although FEM tends to be computationally intensive, the trend of constantly increasing speed and memory resources of modern computers favors FEM over faster simulation techniques that rely on more restrictive simplifications and approximations. Because FEM is a strictly numerical technique, it may provide somewhat limited insight into the underlying physics. However, the strong benefit of FEM is in its innate capability to accommodate complicated geometries, different materials, piezoelectricity, and full crystal anisotropy. Hence, only few simplifying approximations are required, resulting in a precise and flexible simulation technique.

In this paper, we briefly review the FEM formulation for linear forced piezoelectric vibrations using two approaches: 1) the harmonic analysis in which sinusoidal excitation and, consequently, sinusoidal variation of all of the fields are assumed and 2) a modal analysis in which the generalized piezoelectric eigenvalue problem is solved, resulting in the natural frequencies and associated mode shapes within the frequency range of interest. Next, implementation aspects are discussed, such as the memory management method and solution algorithms, which are essential for reducing the required computational effort.

The FEM analysis is applied to membrane-type resonator models, and it is found that only 3D modeling permits detailed information on the pertinent rich mode spectra. Next, the effects of the top electrode geometry on the resonator behavior are studied, which also calls for full 3D analysis. To validate the modeling technique, simulated displacement profiles for resonators featuring square and circular top electrode shapes are compared with those measured from SMR using laser interferometry [29].

II. FINITE ELEMENT FORMULATION FOR LINEAR FORCED VIBRATIONS OF PIEZOELECTRIC MATERIALS

The present section briefly summarizes the essential equations in the FEM formulation for piezoelectric media. For details, see [30], [31]. The governing equations are

$$\nabla \cdot \bar{\mathbf{T}} + \mathbf{f} = \rho \ddot{\mathbf{u}} \text{ and} \quad (1)$$

$$\nabla \cdot \mathbf{D} = \sigma \quad (2)$$

where ρ is the density [kg/m³], $\bar{\mathbf{T}}$ is the mechanical stress tensor [N/m²], \mathbf{f} denotes the mechanical body force [N/m³], \mathbf{D} is the electric displacement vector [C/m²], \mathbf{u} is the mechanical displacement vector [m], and σ abbreviates the (free) volume charge density [C/m³].¹ The piezoelectric constitutive equations that couple the mechanical and electrical quantities in the piezoelectric material are expressed using the abbreviated matrix notation as [32], [33].

$$\mathbf{T}_{6 \times 1} = \mathbf{c}_{6 \times 6}^E \mathbf{S}_{6 \times 1} + \mathbf{e}_{6 \times 3}^T \nabla \phi_{3 \times 1} \text{ and} \quad (3)$$

$$\mathbf{D}_{3 \times 1} = \mathbf{e}_{3 \times 6} \mathbf{S}_{6 \times 1} - \epsilon_{3 \times 3}^S \nabla \phi_{3 \times 1} \quad (4)$$

where \mathbf{T} is the stress column, \mathbf{S} the strain column, ϕ the electric potential [V], \mathbf{e} the piezoelectric matrix [C/m²], \mathbf{c}^E the elastic stiffness matrix (evaluated at constant electric field) [N/m²], and ϵ^S is the dielectric permittivity matrix (evaluated at constant strain) [F/m]. The superscript T denotes the transpose of a matrix. Because the velocity of the electromagnetic wave is five orders of magnitude higher than that of the acoustic wave, the quasi-static approximation $\mathbf{E} = -\nabla \phi$ for the electric field \mathbf{E} [V/m] may be used in (3) and (4) with $\nabla = (\partial/\partial x_1, \partial/\partial x_2, \partial/\partial x_3)^T$. The strain column is related to the mechanical displacement vector \mathbf{u} through

$$\mathbf{S} = \nabla_S \mathbf{u} \quad (5)$$

where

$$\nabla_S = \begin{bmatrix} \frac{\partial}{\partial x_1} & 0 & 0 \\ 0 & \frac{\partial}{\partial x_2} & 0 \\ 0 & 0 & \frac{\partial}{\partial x_3} \\ 0 & \frac{\partial}{\partial x_3} & \frac{\partial}{\partial x_2} \\ \frac{\partial}{\partial x_3} & 0 & \frac{\partial}{\partial x_1} \\ \frac{\partial}{\partial x_2} & \frac{\partial}{\partial x_1} & 0 \end{bmatrix}. \quad (6)$$

For a unique solution, the mechanical (for displacement or stress) and electrical (for electric potential or electric displacement) boundary conditions need to be imposed on the entire boundary of the problem domain. The boundary conditions, together with (1)–(6), then completely determine the motion of the piezoelectric material. Alternative equivalent representation of this boundary value problem is in terms of Hamilton's variational principle [34], [35]. This is especially useful in the derivation of various approximate formulations (see [36] and [37]).

A. Discretization

Consider a volume V constituting the problem domain as illustrated in Fig. 2 for a BAW resonator. In FEM, the physical problem domain V is discretized, i.e., subdivided into small elementary volumes called elements. The continuous field quantities—the three components of the mechanical displacement u_i , $i = 1, 2, 3$ and the electric

¹With $\sigma = 0$ as an insulating material.

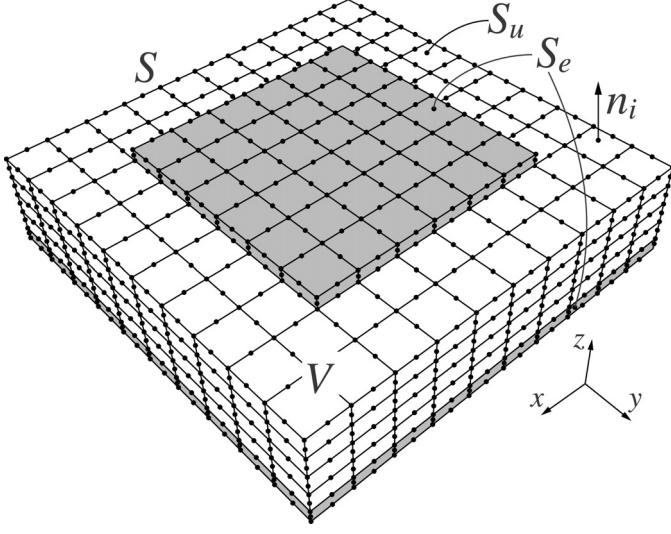


Fig. 2. Simple BAW resonator defining the problem domain V . For clarity, only the part of the volume-element mesh located on the boundary S of volume V is shown. The boundary S with unit outward normal n_i is divided into two parts: the part covered with electrodes S_e and the remaining non-metalized part S_u . The piezoelectric material (white) is between two electrodes (gray).

potential ϕ —are approximated in each element through linear sums of interpolation functions (shape functions):

$$\begin{cases} u_i(\mathbf{r}) = \sum_{j=1}^n a_{ij} N_j(\mathbf{r}), & i = 1, 2, 3, \\ \phi(\mathbf{r}) = \sum_{j=1}^n b_j N_j(\mathbf{r}), & \mathbf{r} \in V_e. \end{cases} \quad (7)$$

Here $\mathbf{r} = (x_1, x_2, x_3)^T$ is the position vector, n is the number of specific so-called “node points” of the element, and a_{ij} and b_j are the displacement and electrical degrees of freedom (DOF), respectively. The DOFs are the unknowns, whose values finally result from the solution of the FEM equations.

In (7), $N_j(\mathbf{r}) = N_j(x_1, x_2, x_3)$ are the shape functions (chosen to be polynomials) associated with the element, and they satisfy the interpolation property

$$N_j(\mathbf{r}_i) = N_j(x_{i1}, x_{i2}, x_{i3}) = \delta_{ij}, \quad i, j = 1, \dots, n \quad (8)$$

where \mathbf{r}_i is the location of node point i , and δ_{ij} is the Kronecker delta. This implies that the DOFs equal the values of the field variables at the nodes.

In matrix form, (7) may be expressed as

$$\mathbf{u}(\mathbf{r})_{3 \times 1} = \mathbf{N}_u(\mathbf{r})_{3 \times 3n} \mathbf{a}_{3n \times 1}, \quad \phi(\mathbf{r}) = \mathbf{N}_p(\mathbf{r})_{1 \times n} \mathbf{b}_{n \times 1} \quad (9)$$

where $\mathbf{N}_u(\mathbf{r})$ and $\mathbf{N}_p(\mathbf{r})$ are matrices of shape functions and \mathbf{a} and \mathbf{b} are the column vectors of mechanical and electrical DOFs, respectively.

B. Finite Element Equations

The element equations in matrix form are [4], [31], [38]

$$\begin{bmatrix} \mathbf{k}_{uu} & \mathbf{k}_{u\phi} \\ \mathbf{k}_{u\phi}^T & \mathbf{k}_{\phi\phi} \end{bmatrix} \begin{bmatrix} \mathbf{a} \\ \mathbf{b} \end{bmatrix} + \begin{bmatrix} \mathbf{m}_{uu} & \mathbf{0} \\ \mathbf{0} & \mathbf{0} \end{bmatrix} \begin{bmatrix} \ddot{\mathbf{a}} \\ \ddot{\mathbf{b}} \end{bmatrix} + \begin{bmatrix} \mathbf{g}_{uu} & \mathbf{0} \\ \mathbf{0} & \mathbf{0} \end{bmatrix} \begin{bmatrix} \dot{\mathbf{a}} \\ \dot{\mathbf{b}} \end{bmatrix} = \begin{bmatrix} \hat{\mathbf{F}}_b + \hat{\mathbf{F}}_n + \hat{\mathbf{F}}_p \\ \hat{\mathbf{Q}}_b + \hat{\mathbf{Q}}_n + \hat{\mathbf{Q}}_p \end{bmatrix} \quad (10)$$

where

$$\begin{aligned} \mathbf{k}_{uu} &= \int_e \mathbf{B}_u^T \mathbf{c} \mathbf{B}_u dV \\ \mathbf{k}_{u\phi} &= \int_e \mathbf{B}_u^T \mathbf{e}^T \mathbf{B}_\phi dV \\ \mathbf{k}_{\phi\phi} &= - \int_e \mathbf{B}_\phi^T \boldsymbol{\epsilon} \mathbf{B}_\phi dV \\ \mathbf{m}_{uu} &= \int_e \rho \mathbf{N}_u^T \mathbf{N}_u dV \\ \mathbf{g}_{uu} &= \int_e \mathbf{B}_u^T \boldsymbol{\eta} \mathbf{B}_u dV \\ \hat{\mathbf{F}}_n &= \oint_e \mathbf{N}_u^T \mathbf{t}_n dS \\ \hat{\mathbf{F}}_b &= \int_e \mathbf{N}_u^T \mathbf{f} dV \\ \hat{\mathbf{F}}_p &= \sum \mathbf{N}_u^T(\mathbf{r}_{p_j}) \mathbf{f}_{p_j} \\ \hat{\mathbf{Q}}_n &= - \oint_e \mathbf{N}_p^T q dS \\ \hat{\mathbf{Q}}_b &= - \int_e \mathbf{N}_p^T \sigma dV \\ \hat{\mathbf{Q}}_p &= - \sum \mathbf{N}_p^T(\mathbf{r}_{p_j}) \sigma_{p_j}. \end{aligned} \quad (11)$$

Here, \mathbf{f}_{p_j} is the mechanical point force at position \mathbf{r}_{p_j} , σ_{p_j} is the point charge at the position \mathbf{r}_{p_j} , $\mathbf{t}_n = (\sum_{j=1}^3 T_{1j} n_j, \sum_{j=1}^3 T_{2j} n_j, \sum_{j=1}^3 T_{3j} n_j)^T$ is the mechanical surface force (the traction) (T_{ij} is the stress tensor element and n_j is the j th component of the unit outward normal to the element boundary), and $q = -D_n = -D_j n_j$ is the inward-normal component of the electric displacement on the element boundary. In (11), the definitions $\mathbf{B}_u = \nabla_s \mathbf{N}_u$ and $\mathbf{B}_\phi = \nabla \mathbf{N}_p$ are used. The frequency-dependent mechanical damping is introduced through damping matrix \mathbf{g}_{uu} , where $\boldsymbol{\eta}$ denotes the viscosity matrix [Ns/m²] [39]. Alternatively, frequency-independent mechanical, electric, and piezoelectric losses may be modeled by using complex material constants [40], [41].

These equations apply for each element. The equations describing the whole system, the so-called system equations, are assembled by evaluating contributions of the form of (10) and (11) from each element and adding each matrix element to the appropriate location in the global mass, mechanical stiffness, piezoelectric, dielectric, and damping matrices. The assembly of the system equations is, effectively, the enforcement of continuity of the solution at the interelement boundaries [1]. The form of the resulting linear system of equations to be solved, describing the

whole system, is the same as that of (10). For a mesh with N nodes, the total number of equations is $4N$, with N equations for each field variable.²

C. Boundary Conditions

On the entire boundary of the domain (S in Fig. 2), one needs to define either a natural or an essential boundary condition (BC). For the mechanical quantities, these are expressed, respectively, as

$$(\mathbf{t}_n)_i = \sum_{j=1}^3 T_{ij} n_j - \sum_k (\mathbf{f}_{pk})_i \delta(\mathbf{r} - \mathbf{r}_{pk}) = (\bar{\mathbf{t}}_n)_i \quad (12)$$

or

$$u_i = \bar{u}_i \text{ on } S. \quad (13)$$

Here, \mathbf{f}_{pk} is the mechanical point force at position \mathbf{r}_{pk} on the surface S and δ is the Dirac delta function. The sum k is over the point forces. Furthermore, \bar{u}_i and $(\bar{\mathbf{t}}_n)_i$ (with $i = 1, 2, 3$) are the prescribed components of displacement and surface traction, respectively, and n_j denote the components of the unit outward normal to the domain boundary.

The electrical BCs are expressed through

$$q = - \sum_{j=1}^3 D_{ij} n_j - \sum_k \rho_{pk} \delta(\mathbf{r} - \mathbf{r}_{pk}) = \bar{D}_n \quad (14)$$

or

$$\phi = \bar{\phi} \text{ on } S, \quad (15)$$

where $\bar{\phi}$ is the prescribed potential, and ρ_{pk} denotes the point charge at position \mathbf{r}_{pk} on the surface S . The sum k is over the point charges. On the dielectric part of the boundary (S_u in Fig. 2), \bar{D}_n is the prescribed inward normal component of the electric displacement. On the part of the piezoelectric material boundary covered with electrodes, \bar{D}_n is replaced with the prescribed surface charge density $\bar{\sigma}$.

In the 2D case, the field variables are assumed independent of the x_2 -direction, i.e., we are considering straight-crested waves. Hence, the 2D case is obtained readily by setting all of the derivatives with respect to x_2 to 0 ($\frac{\partial}{\partial x_2} \equiv 0$) and replacing the volume and surface integrals, respectively, with surface and line integrals. The line integral then extends over the boundary of the element in the counterclockwise direction. In addition, in 2D modeling, we usually take the x_2 displacement to vanish such that the motion is in the plane only.

²Application of the essential boundary conditions is implemented through appropriate manipulation of the matrices in the system equations involving the removal of matrix rows and columns. Hence, the number of equations to be finally solved is usually less than $4N$.

III. HARMONIC ANALYSIS

For the time harmonic case, sinusoidal variation of the physical quantities is assumed, i.e., $\mathbf{a}, \mathbf{b} \propto e^{i\omega t}$. Then, after application of the BCs, the resulting system equations may be represented by

$$\begin{bmatrix} \mathbf{K}_{uu} & \mathbf{K}_{u\phi} & \mathbf{K}_{uF} & \mathbf{K}_{uQ} \\ \mathbf{K}_{u\phi}^T & \mathbf{K}_{\phi\phi} & \mathbf{K}_{\phi F} & \mathbf{K}_{\phi Q} \\ \mathbf{K}_{uF}^T & \mathbf{K}_{\phi F}^T & \mathbf{K}_{FF} & \mathbf{K}_{FQ} \\ \mathbf{K}_{uQ}^T & \mathbf{K}_{\phi Q}^T & \mathbf{K}_{FQ}^T & \mathbf{K}_{QQ} \end{bmatrix} \begin{bmatrix} \mathbf{a} \\ \mathbf{b} \\ \mathbf{a}_F \\ \mathbf{b}_Q \end{bmatrix} - \omega^2 \begin{bmatrix} \mathbf{M}_{uu} & \mathbf{0} & \mathbf{M}_{uF} & \mathbf{0} \\ \mathbf{0} & \mathbf{0} & \mathbf{0} & \mathbf{0} \\ \mathbf{M}_{uF}^T & \mathbf{0} & \mathbf{M}_{FF} & \mathbf{0} \\ \mathbf{0} & \mathbf{0} & \mathbf{0} & \mathbf{0} \end{bmatrix} \begin{bmatrix} \mathbf{a} \\ \mathbf{b} \\ \mathbf{a}_F \\ \mathbf{b}_Q \end{bmatrix} + i\omega \begin{bmatrix} \mathbf{G}_{uu} & \mathbf{0} & \mathbf{G}_{uF} & \mathbf{0} \\ \mathbf{0} & \mathbf{0} & \mathbf{0} & \mathbf{0} \\ \mathbf{G}_{uF}^T & \mathbf{0} & \mathbf{G}_{FF} & \mathbf{0} \\ \mathbf{0} & \mathbf{0} & \mathbf{0} & \mathbf{0} \end{bmatrix} \begin{bmatrix} \mathbf{a} \\ \mathbf{b} \\ \mathbf{a}_F \\ \mathbf{b}_Q \end{bmatrix} = \begin{bmatrix} \mathbf{F} \\ \mathbf{Q} \\ \mathbf{F}_F \\ \mathbf{Q}_Q \end{bmatrix}. \quad (16)$$

The FEM equations in (16) are partitioned such that those rows and columns corresponding to DOFs with an essential BC imposed are grouped together (submatrices with subscripts \mathbf{F} and \mathbf{Q}). The column vectors of prescribed nodal displacement and potential are \mathbf{a}_F and \mathbf{b}_Q , respectively. The column vectors \mathbf{F} and \mathbf{Q} , respectively, are those of mechanical force and electric charge. From the first two equations, the FEM equations to be solved may be expressed compactly as

$$[\mathbf{K} - \omega^2 \mathbf{M} + i\omega \mathbf{G}] \mathbf{x} = \mathbf{F}_{h0} \quad (17)$$

where

$$\begin{aligned} \mathbf{K} &= \begin{bmatrix} \mathbf{K}_{uu} & \mathbf{K}_{u\phi} \\ \mathbf{K}_{u\phi}^T & \mathbf{K}_{\phi\phi} \end{bmatrix}, \quad \mathbf{M} = \begin{bmatrix} \mathbf{M}_{uu} & \mathbf{0} \\ \mathbf{0} & \mathbf{0} \end{bmatrix}, \\ \mathbf{G} &= \begin{bmatrix} \mathbf{G}_{uu} & \mathbf{0} \\ \mathbf{0} & \mathbf{0} \end{bmatrix}, \quad \mathbf{x} = \begin{bmatrix} \mathbf{a} \\ \mathbf{b} \end{bmatrix}, \text{ and} \\ \mathbf{F}_{h0} &= \begin{bmatrix} \mathbf{F} \\ \mathbf{Q} \end{bmatrix} - \left(\begin{bmatrix} \mathbf{K}_{uF} & \mathbf{K}_{uQ} \\ \mathbf{K}_{\phi F} & \mathbf{K}_{\phi Q} \end{bmatrix} - \omega^2 \begin{bmatrix} \mathbf{M}_{uF} & \mathbf{0} \\ \mathbf{0} & \mathbf{0} \end{bmatrix} + i\omega \begin{bmatrix} \mathbf{G}_{uF} & \mathbf{0} \\ \mathbf{0} & \mathbf{0} \end{bmatrix} \right) \begin{bmatrix} \mathbf{a}_F \\ \mathbf{b}_Q \end{bmatrix}. \end{aligned} \quad (18)$$

The electromechanical stiffness matrix \mathbf{K} is indefinite; the mass matrix \mathbf{M} is positive semidefinite [42].

In harmonic analysis, (17) is solved for the unknowns \mathbf{x} —the displacement and potential DOFs at the given frequency ω . From the solution, the element stress and electric displacement may be further obtained as

$$\mathbf{T} = \mathbf{c} \mathbf{B}_u \mathbf{a} + \mathbf{e}^T \mathbf{B}_\phi \mathbf{b} \text{ and} \quad (19)$$

$$\mathbf{D} = \mathbf{e} \mathbf{B}_u \mathbf{a} - \epsilon \mathbf{B}_\phi \mathbf{b}, \quad (20)$$

respectively.

A. Admittance

The admittance Y is obtained through dividing total charge Q on an electrode by the amplitude of the driving voltage V :

$$Y(\omega) = \frac{i\omega Q}{V}. \quad (21)$$

The total charge on the electrode is computed as a sum of nodal charges. Inserting the solved DOFs into (16), the so-called vector of reactions $[\mathbf{F}_F^T \mathbf{Q}_Q^T]^T$ is obtained. Here, \mathbf{F}_F is the nodal force at the nodes with fixed displacement, and \mathbf{Q}_Q is the nodal charge at nodes with fixed potential. The total charge on a given electrode is computed through summing the nodal charges:

$$Q = -\mathbf{I}_{el}^T \mathbf{Q}_Q \quad (22)$$

where \mathbf{I}_{el} is a vector with unity at positions corresponding to those electrical DOFs that belong to the given electrode, and zeros elsewhere. The minus sign results from the definition of the current as positive into the piezoelectric body.

Computing the frequency response (e.g., admittance vs. frequency) requires the solution of the FEM equations at each of the desired frequencies. An alternative approach exploits the fact that the solution can be represented through a superposition of only a limited number of relevant modes that are excited in the frequency range considered [1], [43]. This approach involves the solution of the natural frequencies of the structure and the associated eigenmodes and is described in the next section.

IV. MODAL ANALYSIS

In modal analysis, the generalized piezoelectric eigenvalue problem formed by setting the load vector \mathbf{F}_{ho} and damping matrix \mathbf{G} equal to zero in (17) is solved for the eigenpairs, i.e., eigenvalues (resonance frequencies) and eigenvectors (mode shapes). We consider mainly the case of voltage loading, i.e., one electrode is electrically grounded, and a sinusoidal voltage with prescribed constant amplitude is connected between the grounded and “hot” electrode. Solution of the eigenvalue problem then results in series resonance frequencies (short-circuited electrodes) at which the electrical impedance assumes low values. The parallel resonance frequencies with large values of impedance can be obtained from the open-circuited case [30], [44]. For the open-circuit boundary conditions, the potential is set constant on the “hot” electrode, but not fixed (floating potential).³

In practice, because of increased computing times, it is not possible to solve for all of the eigenpairs for large problems. Instead, the modes are only computed in the frequency range of interest, e.g., in the vicinity of the fundamental thickness extensional mode. Because only part of the modes are taken into account, the electrical and mechanical responses obtained with modal analysis are approximations of those computed with the harmonic analysis.

³The piezoelectric material between the two electrodes also forms a waveguide for electromagnetic waves. The assumption of a uniform potential on the electrodes implies that 1) the frequencies are low enough, such that the wavelength of the EM wave propagating in the waveguide is much larger than the lateral dimensions of the resonator and 2) the electrode is a perfect conductor.

A. Generalized Piezoelectric Eigenvalue Problem

The derivation of the subsequent equations closely follows that in [45]. Assuming harmonic motion and no damping, (16) takes the form

$$\left(\begin{bmatrix} \mathbf{K}_{uu} & \mathbf{K}_{u\phi} & \mathbf{K}_{u0} \\ \mathbf{K}_{\phi u}^T & \mathbf{K}_{\phi\phi} & \mathbf{K}_{\phi 0} \\ \mathbf{K}_{0u}^T & \mathbf{K}_{0\phi}^T & \mathbf{K}_{00} \end{bmatrix} - \omega^2 \begin{bmatrix} \mathbf{M}_{uu} & \mathbf{0} & \mathbf{M}_{u0} \\ \mathbf{0} & \mathbf{0} & \mathbf{0} \\ \mathbf{M}_{0u}^T & \mathbf{0} & \mathbf{M}_{00} \end{bmatrix} \right) \times \begin{bmatrix} \mathbf{a} \\ \mathbf{b} \\ \mathbf{e}_0 \end{bmatrix} = \begin{bmatrix} \mathbf{F}_0 \\ \mathbf{Q}_0 \\ \mathbf{F}_R \end{bmatrix} \quad (23)$$

where, using the submatrices in (16),

$$\begin{aligned} \mathbf{K}_{u0} &= [\mathbf{K}_{uF} \ \mathbf{K}_{uQ}] & \mathbf{K}_{\phi 0} &= [\mathbf{K}_{\phi F} \ \mathbf{K}_{\phi Q}] \\ \mathbf{K}_{00} &= \begin{bmatrix} \mathbf{K}_{FF} & \mathbf{K}_{FQ} \\ \mathbf{K}_{FQ}^T & \mathbf{K}_{QQ} \end{bmatrix} & \mathbf{M}_{u0} &= [\mathbf{M}_{uF} \ \mathbf{0}] \\ \mathbf{M}_{00} &= \begin{bmatrix} \mathbf{M}_{FF} & \mathbf{0} \\ \mathbf{0} & \mathbf{0} \end{bmatrix} & \mathbf{e}_0 &= \begin{bmatrix} \mathbf{a}_F \\ \mathbf{b}_Q \end{bmatrix}. \end{aligned} \quad (24)$$

In (23), \mathbf{F}_R is the vector of reactions. The first two equations in (23) may be written as

$$\left(\begin{bmatrix} \mathbf{K}_{uu} & \mathbf{K}_{u\phi} \\ \mathbf{K}_{\phi u} & \mathbf{K}_{\phi\phi} \end{bmatrix} - \omega^2 \begin{bmatrix} \mathbf{M}_{uu} & \mathbf{0} \\ \mathbf{0} & \mathbf{0} \end{bmatrix} \right) \begin{bmatrix} \mathbf{a} \\ \mathbf{b} \end{bmatrix} = \begin{bmatrix} \mathbf{F}_0 \\ \mathbf{Q}_0 \end{bmatrix} \quad (25)$$

where

$$\begin{bmatrix} \mathbf{F}_0 \\ \mathbf{Q}_0 \end{bmatrix} = \begin{bmatrix} \mathbf{F} \\ \mathbf{Q} \end{bmatrix} - \left(\begin{bmatrix} \mathbf{K}_{u0} \\ \mathbf{K}_{\phi 0} \end{bmatrix} - \omega^2 \begin{bmatrix} \mathbf{M}_{u0} \\ \mathbf{0} \end{bmatrix} \right) \mathbf{e}_0 \quad (26)$$

is the equivalent load that converts the applied displacement and voltage loading to mechanical force and electrical charge on the nodes of the FEM mesh. The associated generalized eigenvalue problem is

$$\begin{bmatrix} \mathbf{K}_{uu} & \mathbf{K}_{u\phi} \\ \mathbf{K}_{\phi u} & \mathbf{K}_{\phi\phi} \end{bmatrix} \begin{bmatrix} \mathbf{u}_u \\ \mathbf{u}_\phi \end{bmatrix} - \begin{bmatrix} \mathbf{M}_{uu} & \mathbf{0} \\ \mathbf{0} & \mathbf{0} \end{bmatrix} \begin{bmatrix} \mathbf{u}_u \\ \mathbf{u}_\phi \end{bmatrix} [\Omega^2] = \begin{bmatrix} \mathbf{0} \\ \mathbf{0} \end{bmatrix} \quad (27)$$

where $\mathbf{u} = [\mathbf{u}_u^T \ \mathbf{u}_\phi^T]^T$ is the matrix of eigenvectors (mode shapes) corresponding to the mechanical DOFs; $[\Omega^2]$ denotes the diagonal matrix of the corresponding eigenvalue spectrum. The electrical DOFs have zero mass and, consequently, infinite eigenvalues associated with them [45]; the eigenvectors corresponding to electrical DOFs may be neglected. The eigenvectors are normalized:

$$\mathbf{u}_u^T \mathbf{M}_{uu} \mathbf{u}_u = \mathbf{I}; \quad \mathbf{u}^T \begin{bmatrix} \mathbf{K}_{uu} & \mathbf{K}_{u\phi} \\ \mathbf{K}_{\phi u} & \mathbf{K}_{\phi\phi} \end{bmatrix} \mathbf{u} = [\Omega^2]. \quad (28)$$

The unknown mechanical and electrical DOFs at the frequency ω can be expressed in terms of the solved eigenvectors and eigenvalues.

B. Mechanical and Electrical Response

For voltage excitation, one electrode is grounded, and a potential φ is imposed on the “hot” electrode. Then, the displacement vector may be written as

$$\mathbf{a} = \sum_{j=1}^n \frac{\mathbf{u}_{u_j} \varphi H_j}{\omega_j^2 - \omega^2 + i\eta_j \omega_j^2}, \quad (29)$$

and the potential vector may be written as

$$\mathbf{b} = \sum_{j=1}^n \frac{\mathbf{u}_{\phi_j} \varphi H_j}{\omega_j^2 - \omega^2 + i\eta_j \omega_j^2} + \mathbf{K}_{\phi\phi}^{-1} \mathbf{Q}_0. \quad (30)$$

In (29) and (30), \mathbf{u}_{u_j} and \mathbf{u}_{ϕ_j} are, respectively, the mechanical and electrical parts of the eigenvector corresponding to the eigenvalue ω_j , and

$$H_j = \frac{1}{\varphi} \begin{bmatrix} \mathbf{u}_u \\ \mathbf{u}_\phi \end{bmatrix}_j^T \begin{bmatrix} \mathbf{F}_0 \\ \mathbf{Q}_0 \end{bmatrix}. \quad (31)$$

In the denominators of (29) and (30), damping is introduced through term $i\eta_j \omega_j^2$, where η_j describes the strength of damping in mode j .

Inserting \mathbf{a} and \mathbf{b} into (23), \mathbf{F}_R , the column of reactions, can be computed. The total charge on the electrode at the potential φ is obtained through summing the nodal charge: $Q_T = -\mathbf{I}_Q^T \mathbf{F}_R$, where \mathbf{I}_Q^T is a row vector with unity at the positions corresponding to the electrical DOFs associated with nodes on the electrode at the potential φ and zeros elsewhere. The admittance may be expressed as

$$Y(\omega) = \sum_{j=1}^n \frac{i\omega M_j}{\omega_j^2 - \omega^2 + i\eta_j \omega_j^2} + i\omega C_p \quad (32)$$

where the modal constants M_j , defined as

$$M_j = -\mathbf{I}_Q^T [\mathbf{K}_{u0}^T \mathbf{K}_{\phi 0}^T] \begin{bmatrix} \mathbf{u}_u \\ \mathbf{u}_\phi \end{bmatrix}_j H_j, \quad (33)$$

indicate the contribution of mode j to the electrical response [45], [46]. The shunt capacitance C_p is given by

$$C_p = -\frac{1}{\varphi} \mathbf{I}_Q^T [\mathbf{K}_{00} \mathbf{e}_0 + \mathbf{K}_{\phi 0}^T \mathbf{K}_{\phi\phi}^{-1} \mathbf{Q}_0]. \quad (34)$$

For the case $\mathbf{F} = \mathbf{Q} = \mathbf{0}$ in (23) and with the prescribed values of mechanical DOFs in the vector \mathbf{e}_0 equal to zero, one obtains $M_j = H_j^2$. As already mentioned, the admittance in (32) approximates that obtained using the harmonic analysis approach in the case that only part of the modes are included in the sum, i.e., if $n < N_u$, where N_u is the total number of free mechanical DOFs (number of elements in the column vector \mathbf{a}). The same holds for the solved displacement and potential in (29) and (30), respectively.

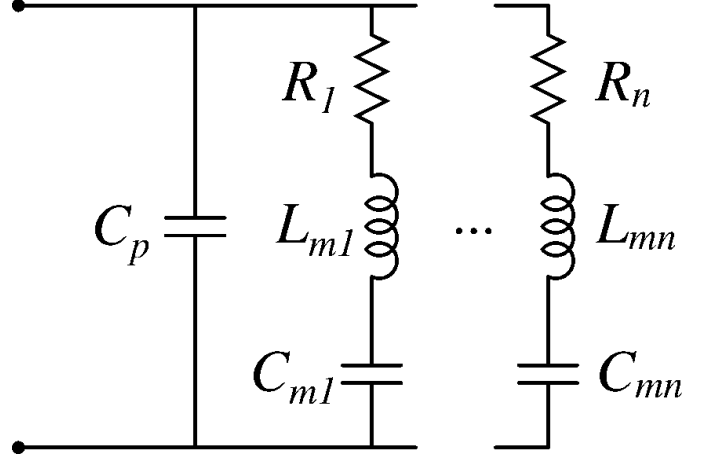


Fig. 3. Extended Butterworth Van Dyke lumped element equivalent circuit of a BAW resonator [20].

C. Equivalent Circuit Representation

Consider the extended Butterworth Van Dyke lumped element equivalent circuit of a BAW resonator [20] shown in Fig. 3. Each branch contains a resistor, an inductor, and a capacitor, representing a resonance in the frequency response of the resonator. The admittance of the equivalent circuit is

$$Y(\omega) = \sum_{j=1}^n \frac{\frac{i\omega}{L_{mj}}}{\frac{1}{L_{mj}C_{mj}} - \omega^2 + i\omega \frac{R_j}{L_{mj}}} + i\omega C_p. \quad (35)$$

Defining the unloaded quality factor of the series resonance as $Q_{sj} = 1/(\omega_j C_{mj} R_j)$ [20], gives $R_j/L_{mj} = \omega_j/Q_{sj}$. Comparing (32) and (35) allows one to express the equivalent circuit elements in terms of the FEM modal analysis parameters:

$$C_{mj} = \frac{M_j}{\omega_j^2} \quad (36)$$

$$L_{mj} = \frac{1}{M_j} \quad (37)$$

$$R_j = \frac{\omega_j \eta_j}{M_j}, \quad Q_{sj} = \frac{1}{\eta_j} \quad (38)$$

$$\omega_j = \frac{1}{\sqrt{L_{mj} C_{mj}}}. \quad (39)$$

The intensity of modes is commonly evaluated using the effective piezoelectric coupling coefficient [38], [42]:

$$k_{eff,j} = \sqrt{\frac{\omega_{pj}^2 - \omega_j^2}{\omega_j^2}} \quad (40)$$

with ω_{pj} and ω_j , respectively, denoting the parallel and series resonance frequencies (antiresonance and resonance frequencies). In the idealized case of only one excited mode, say mode j , the parallel resonance frequency ω_{pj}

can be found by omitting other terms in the sum appearing in (32), except the one corresponding to mode j , and setting the admittance equal zero. Omitting the damping factor yields

$$\omega_{pj} = \sqrt{\omega_j^2 + \frac{M_j}{C_p}}. \quad (41)$$

Substitution into (40) leads to

$$k_{eff,j} = \sqrt{\frac{C_{mj}}{C_p}} = \sqrt{\frac{M_j}{\omega_j^2 C_p}}, \quad (42)$$

relating the effective coupling constant $k_{eff,j}$ and modal constant M_j .

V. COMPUTER IMPLEMENTATION

The main features of our FEM software are 1) the use of 2D quadrilateral elements with cubic and 3D brick elements with quadratic interpolation polynomials for improved accuracy of the results, 2) skyline storage scheme utilizing the characteristic sparse structure of the consistent mass matrix, and 3) use of the spectral transformation Lanczos method for efficient solution of the generalized piezoelectric eigenvalue problem. For creation of 2D resonator models, we have developed a separate preprocessor program. For 3D models, the computational mesh needs to be created using a commercial preprocessor program. The 3D FEM meshes of resonators modeled in this paper are created using the preprocessor of the commercially available ANSYS software. For the postprocessing, e.g., visualization of the computed fields and mode shapes, postprocessing programs both for 2D and 3D geometries have been coded. The software is implemented in the C language, although it uses several numerical subroutine libraries programmed in Fortran (such as BLAS, LAPACK, and ARPACK [47]).

Our FEM solver is based on the approach of [1], which is extended appropriately to model piezoelectric materials. The integrals in the element equations (10) are evaluated numerically using Gauss-Legendre quadrature. The order of quadrature may be chosen in the range from 1 to 5. Currently, for 2D modeling, quadrilateral elements up to cubic and, for 3D modeling, linear and quadratic brick elements have been implemented. All of the elements are of serendipity type, i.e., the nodes are located on the boundary of the element. The shape functions are mapped from the parent element on real elements in the actual mesh (isoparametric elements), allowing for curved element boundaries. The vectors required for the computation of the reactions, e.g., $\mathbf{I}_Q^T [\mathbf{K}_{uo}^T \mathbf{K}_{\phi o}^T]$ and $\mathbf{I}_Q^T \mathbf{K}_{oo} \mathbf{e}_o$ in (33) and (34), respectively, are computed at the assembly phase without need to form the full matrices in (16) and (23). The materials properties are defined through the full stiffness, piezoelectric, dielectric, and viscosity constant matrices. In harmonic analysis, local non-uniform

damping may be modeled by spatially varying the viscosity constants.

The application of essential BCs involves modification of the right-hand side in the system equations, as is evident in (18) and (26). The rows and columns associated with the DOFs, where an essential BC is imposed, may be removed from the matrix equations to be solved. The program allows for sets of nodes to be coupled, i.e., a specified field variable is forced to assume the same value on the coupled nodes. Then, all but one of the corresponding DOFs may be eliminated from the system equations, thus slightly reducing the computational task. After the solution, the value obtained for one remaining DOF is copied to the rest of the DOFs in the coupled set. This is convenient, e.g., in defining the driving voltage between two electrodes under the assumption that the potential does not vary over the electrode. Also, configurations involving electrodes without a fixed potential, such as monolithic crystal filters and stacked crystal filters [17] can be modeled. Floating electrodes are treated by coupling the potential of the nodes belonging to the electrode but leaving the value of the potential undetermined; the electrode potential is obtained via the solution of the FEM equations.

A. Skyline Matrix Storage Scheme

The FEM matrices in (17) and (23) are sparse, symmetric, and banded, i.e., most of the elements equal zero, and the nonzero elements are grouped close to the diagonal of the matrix. This results from the local connectivity property of the FEM, as opposed to the global connectivity, e.g., in boundary element method, which leads to dense matrices. The assembly of the global FEM matrix from the element contributions is illustrated in Fig. 4. Because there are four field variables to be considered, each node corresponds to four rows and columns in the FEM matrices. Node i is connected to all of the nodes in those elements that share node i . Hence, in the example shown in Fig. 4, e.g., node 13 is connected to nodes 1–8, 12, 14–15, 17, 18, 20, 21, and 28–31, resulting in non-zero elements at locations shown in dark gray. Because of symmetry, it suffices to save only the upper or lower triangular part.

The sparsity structure of the electromechanical stiffness matrix \mathbf{K} is shown in an expanded view of Fig. 5. In the conventional skyline (envelope) scheme applied to the stiffness matrix, the elements in each column are stored from the diagonal element until the last non-zero element above the diagonal. For the mass matrix, a modified scheme [48] is utilized that exploits its specific structural pattern shown in Fig. 6. The non-vanishing elements are located on the diagonals of 3×3 submatrices; most of the zeros inside the envelope are not stored. The reduction in the number of the stored elements also reduces the number of computational operations, resulting in savings in the execution time.

To minimize the execution time and memory requirements, it is essential to arrange the DOFs in the FEM equations such that the number of elements within the

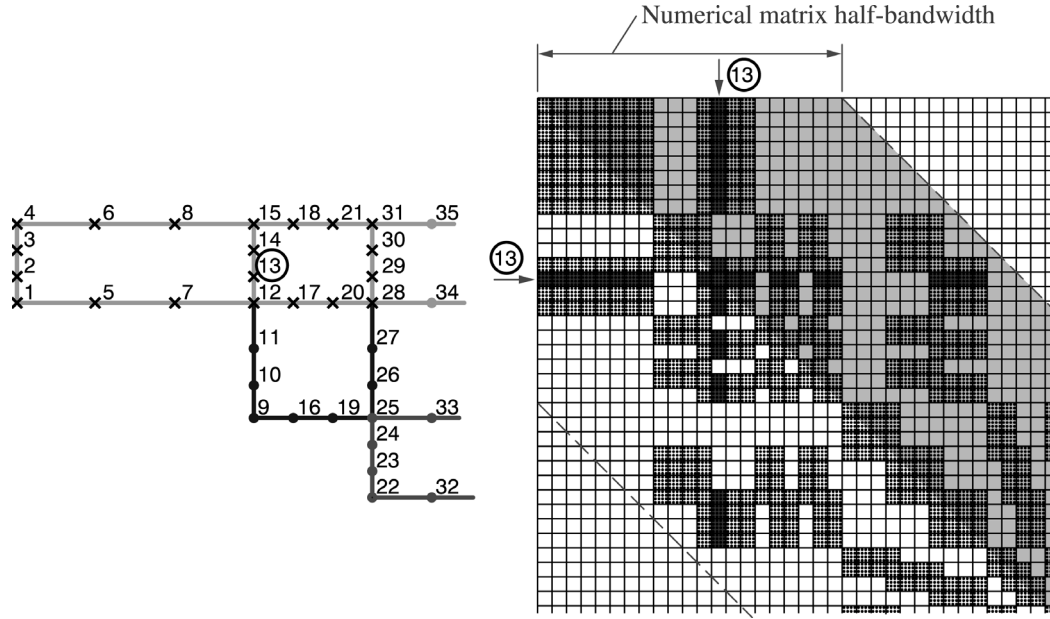


Fig. 4. FEM mesh (left) and the corresponding structure of the electromechanical stiffness matrix \mathbf{K} (right). The grid in the graphical representation of the \mathbf{K} matrix divides it into 4×4 submatrices. The nodes coupled to node number 13 are denoted with crosses in the FEM mesh. The non-zero elements associated with node 13 in the \mathbf{K} matrix potentially are presented in dark gray. Instead of the ordering of the DOFs explicit in (17) and (23), i.e., all of the mechanical DOFs precede the electrical DOFs, the mixed ordering reported in [50], which decreases the matrix bandwidth, is used here: the mechanical DOFs of each node are followed by the electrical DOF of the node.

skyline (matrix profile) is minimized. Prior to the assembly of the system matrices, the node numbering and/or order of the DOFs in the \mathbf{K} matrix are optimized with respect to the matrix profile using the Gibbs-King algorithm [49].⁴ The effect of optimization of the node numbering using the Gibbs-King algorithm on the structure of the electromechanical stiffness matrix \mathbf{K} is plotted in Fig. 7 and 8, showing the significant reduction in the matrix profile.

B. Solution of Generalized Eigenvalue Problem

In the modal analysis, the eigenvalues and eigenvectors of the generalized piezoelectric eigenvalue problem resulting from the FEM formulation are solved using a variant of the Lanczos algorithm, as implemented in the numerical ARPACK library [47]. The efficiency of the method results from the fact that the algorithm retains the banded sparse structure of the stiffness matrix, in contrast to the conventional method, which uses a static condensation technique [4], [30] to eliminate the electric potential DOFs from the equations prior to the solution of the eigenvalue problem [48]. The spectral transformation Lanczos algorithm computes the given number of eigenpairs whose eigenvalues are in the vicinity of a given limit ω_0^2 . Before the iteration starts, the matrix $\mathbf{K} - \omega_0^2 \mathbf{M}$ is formed and factored. In the iteration process, the two major operations required are 1) solution of a linear system of equations with the prefactored coefficient matrix and 2) multiplication of the mass

matrix with a vector.⁵ The solution technique used allows for an efficient computation of the resonance frequencies (eigenvalues) and mode shapes (eigenvectors), especially for resonator configurations that involve narrow matrix bandwidths [50]. This is the case for 2D models of the thin and wide BAW composite resonator structures considered here.

VI. FEM SIMULATIONS OF THIN-FILM RESONATORS

We apply the FEM modeling software to the analysis of the vibration characteristics of membrane type thin-film resonator configurations. The response of the resonator considered is characterized by using the modal analysis approach to compute the resonant frequencies, displacement profiles, and excitation strengths of the modes in the vicinity of the fundamental thickness extensional mode. In thin-film resonators, the thickness of electrodes can be significant in comparison with the total thickness of the resonator. Consequently, ignoring the electrodes or including them in the model merely as additional mass loading, as is done in various plate theories for piezoelectric resonators [36], [37], may result in an inaccurate description. More-

⁴The DOF ordering shown in Fig. 4, 5, and 6 is that before the optimization.

⁵In the Lanczos method described in [48], [50], Cholesky factorization of the mass matrix is required. This will retain the structure of the mass matrix shown in Fig. 6, but many of the zeros on the diagonals of those 3×3 submatrices, which are inside the envelope, would be replaced by non-zero elements. Because a factorization of the mass matrix is not required here, the storage method of the mass matrix could be further improved through saving only the non-zero elements. In this case, e.g., the elements at positions 362, 373, and 384 in Fig. 6 would not be saved.

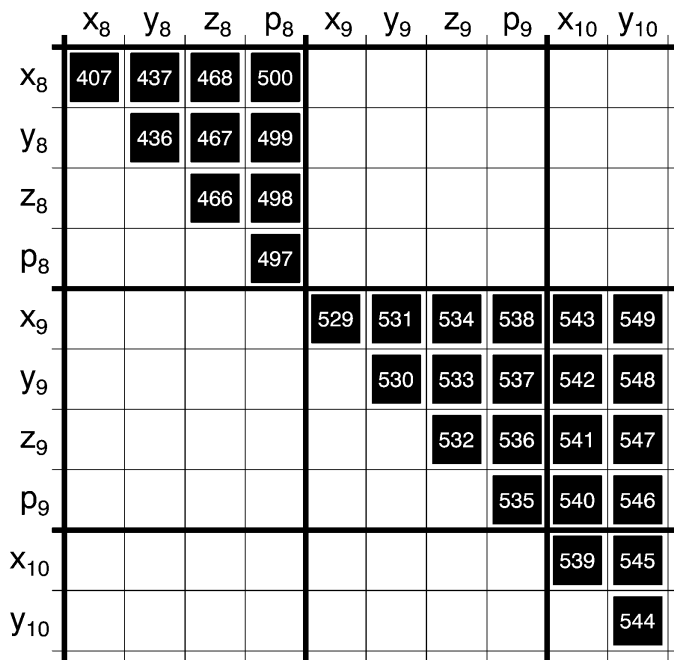


Fig. 5. Sparsity structure of the stiffness matrix. Black squares denote possible nonzero elements. Numbers refer to the position in the vector storing the matrix elements in the skyline scheme. The row and column labels identify the field variables: the displacements (x, y, z) and electric potential (p). The subscript refers to the node number.

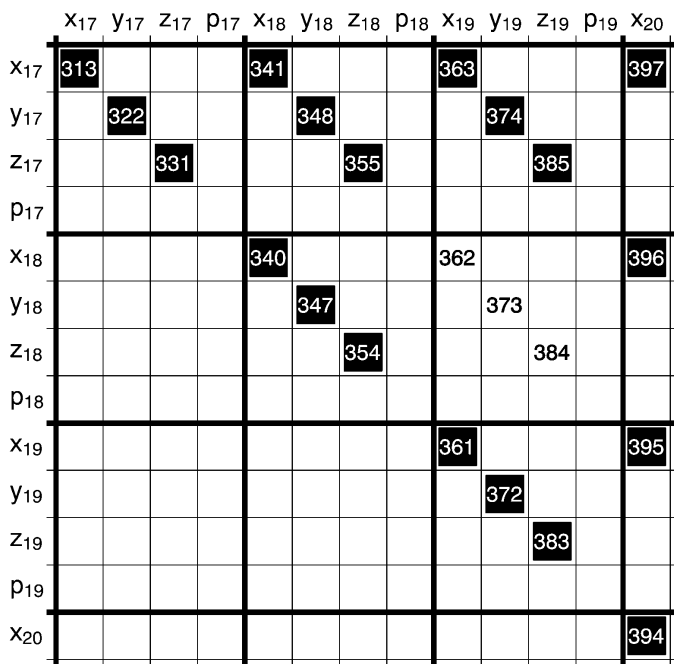


Fig. 6. Structural pattern of the mass matrix; for explanation, see Fig. 5.

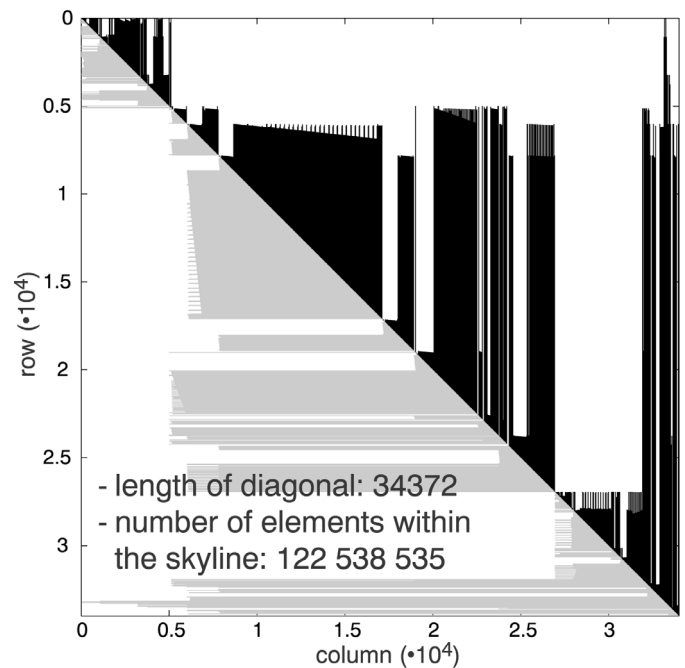


Fig. 7. Skyline of the \mathbf{K} matrix for a 3D FE model without optimization of the node numbering.

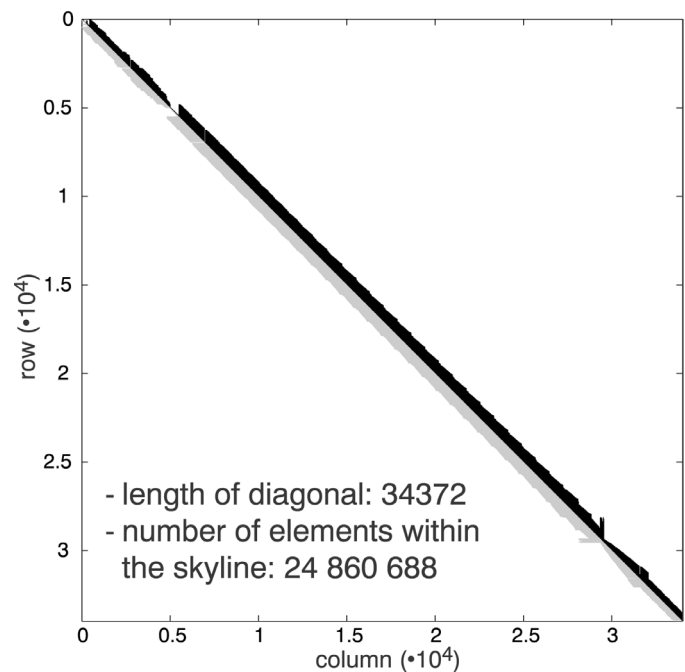


Fig. 8. Skyline of the \mathbf{K} matrix for a 3D FE model with optimization of the node numbering using the Gibbs-King algorithm.

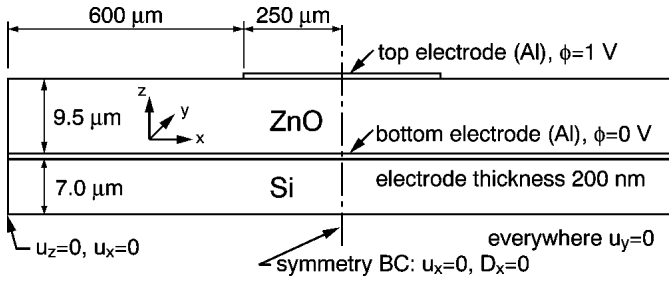


Fig. 9. Materials and dimensions of the membrane BAW composite resonator [53] modeled.

over, the support layers in membrane configurations and the layers in the acoustic mirror in SMR are comparable with the thickness of the piezoelectric. The situation is similar to ultrasonic transducers with matching and backing layers. For their modeling, 3D FEM is widely used [6], [38]. However, the 3D FEM can be computationally exceedingly intensive. To reduce the computational load, laminated plate theories have been suggested for the modeling of thin-film resonators [51], [52], involving the reduction of the 3D equations into 2D through integration over the thickness direction. However, the plate theories provide accurate results only for certain modes within limited frequency ranges. Therefore, we use full 3D FEM, but with relatively coarse meshes to reduce the required computational costs.

For accurate results, a sufficient number of nodal points per wavelength in the highest mode of interest needs to be used in the computational mesh—the number decreases with increasing order of interpolating polynomials used for the element. Choosing the number of elements in the thickness direction such that the thickness mode is accurately modeled and keeping the element aspect ratio small would require a large number of elements in the lateral directions because of the thin and wide structure of the thin-film resonators. However, because of the relatively large lateral wavelength of the anharmonic thickness extensional modes close in frequency to the fundamental mode, relatively coarse element division in the lateral direction can be used. The higher order elements are less affected by the large element aspect ratios, and, in our simulations with quadratic 3D elements, no numerical problems were encountered.

A. Comparison of 2D and 3D Simulations

First, we study the resonator reported by Milsom *et al.* [53], which they have modeled with the mode-matching method. The 2D cross-section of the resonator configuration is shown in Fig. 9. Because of symmetry, in 3D modeling, it suffices to perform the computations using only one quadrant of the actual resonator and to impose appropriate boundary conditions on the symmetry planes. Simulations in 3D are carried out with 20-node quadratic 3D brick elements. The element division in the lateral directions is regular 14×14 elements per side. The number

of elements in the thickness (z) direction in the Si, Al, ZnO, and Al layers is 1, 1, 2, and 1, respectively, with the largest element aspect ratio in the mesh being 125. In 2D simulations, plane-strain elements are employed, i.e., the y dimension is assumed infinite. Air loading is neglected, and the models are truncated on the edges of the membrane, demonstrating one of the shortcomings of FEM—the difficulty in modeling open boundary problems. Several techniques have been proposed for alleviating this problem, such as the infinite element approach [54], [55]. In harmonic analysis, the effect of the wave reflections from the model edges can be reduced by introducing a region with strong damping at the membrane edges. Here, we simply impose zero displacements on the artificial boundary resulting from the truncation, which is an approximation to the actual BC. However, this introduces only minor modeling errors in case of trapped modes, where the displacements on the boundary are negligible. The potential of the upper electrode is assigned the value 1 V, and the bottom electrode is grounded. On the non-metalized boundaries of the problem domain, the BC $D_n = 0$ is implicitly assumed (no electric flux leakage). Actually, D_n should be continuous across the non-metalized part (for insulating materials) of the boundary rather than zero. However, the approximation is fair for piezoelectric materials with either a weak piezoelectric coupling (as for quartz) or a high dielectric constant [22]. For certain geometries, materials, and modes, flux leakage acts to slightly decrease the resonance and antiresonance frequencies, but can affect more considerably the effective coupling coefficient of the mode [*c.f.*, (40)] [42]. The resonator model is always an idealization of the actual structure, which can feature imperfections affecting the resonator behavior. Moreover, as FEM derives the device behavior directly from the device geometry and materials constants, the accuracy of the results also depends on the precision to which these parameters are known.

The modal constants in (33) together with the admittance in (32), computed for the 2D and 3D models are displayed in Fig. 10 as a function of frequency. It is seen that the fundamental thickness extensional mode, with large average displacement in the z direction at the frequency 221.3 MHz in the 2D case and 221.8 MHz in the 3D case, is most strongly excited. The frequency of the main resonance computed with the 3D model is slightly higher than that computed with the 2D model because of the low number of elements in the thickness direction used in the 3D model—the result is not quite fully converged. Several additional responses or side resonances can be recognized in the vicinity of the main resonance. The unwanted modes present in the frequency response degrade the usability of the resonator. Above the main resonance frequency, the weaker spurious modes are associated with the anharmonic thickness extensional modes (resonances in the lateral direction caused by reflections of Lamb waves on the edges of the electrode [56]). The generation of the plate waves can be attributed to the electrode edges. To satisfy the BC at the electrode edge, thickness extensional modes with a

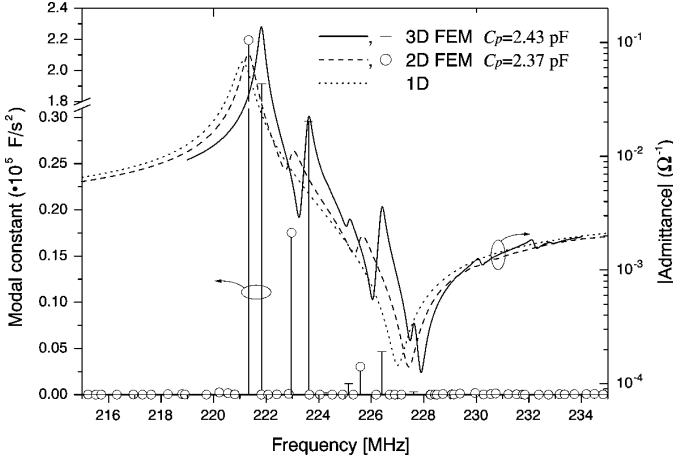


Fig. 10. Modal constants and admittance vs. frequency computed with modal analysis for the 2D and 3D models of the membrane BAW composite resonator. The admittance computed with a 1D model cannot model the parasitic resonances.

non-vanishing lateral component of the wave vector are required. It is clearly seen, by comparing the 2D and 3D results, that the 2D model is not adequate to model the full anharmonic mode content; the 3D model predicts stronger and richer mode spectrum than the 2D model.

The various modes are characterized through their electric and mechanical field profiles. The mechanical field profile is obtained from the mechanical part of the eigenvector. The mode shapes at the main resonance and at selected spurious resonances for the 2D model are shown in Fig. 11. The displacement profiles [computed with (29)] obtained with 3D simulations are plotted at selected resonances in Fig. 12. For the mode in Fig. 11(c), the charge (current) distribution on the upper electrode is also displayed. The electrode effectively integrates the current distribution, resulting in an average current [21]. Hence, the modes with a net current distribution summing up to zero cannot be excited by the applied voltage loading, e.g., in the 2D case, the anharmonic thickness extensional modes with an even number of current (and displacement) maxima across the electroded region are not electrically excited. In other words, because of the symmetry of the resonator geometry, the applied loads, and the materials properties, only symmetric modes can be excited. Both the resonance frequencies and the mode shapes computed with the 2D FEM agree well with those predicted in [53].

All of the plotted modes exhibit energy trapping into the top electrode region, and, hence, the BC of zero displacement at the edges of the membrane is an accurate approximation. Because of the large width-to-thickness ratio of the resonator, Lamb waves propagating in infinite plates can be used to interpret the trapping of the modes. Because the resonance frequency of the mode is above the cut-off frequency of the associated Lamb wave mode for the electroded region, the wave can propagate in the electroded region in the lateral direction (the component of the wave vector in the lateral direction k_x is real). However, the resonance frequency is below the cut-off frequency in

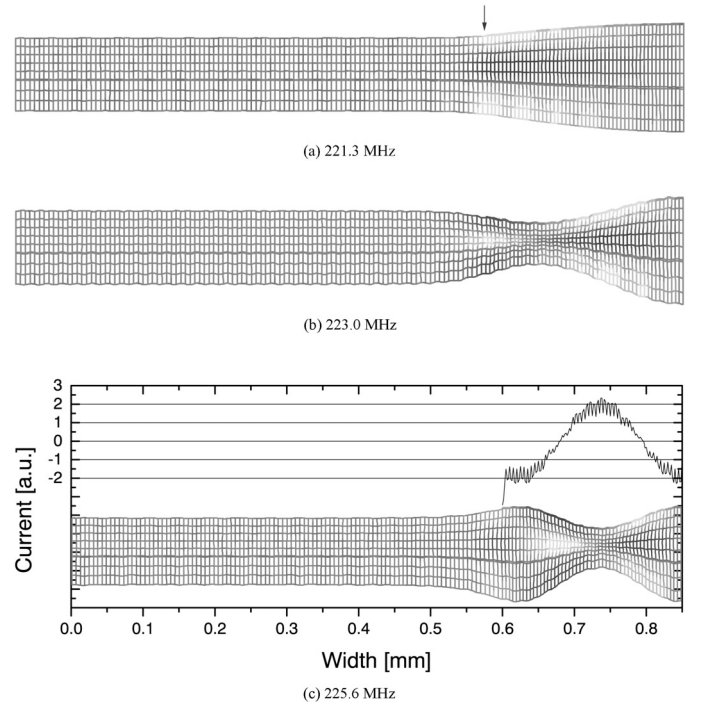


Fig. 11. Modal displacement fields at the selected resonances for the modeled BAW resonator (left half; the right half is symmetric). The arrow marks the edge of the top electrode. The grayscale indicates the lateral displacement. For one of the modes (c), the current distribution in the top electrode is also plotted. The lateral and vertical dimensions are not to scale.

the non-metalized region (imaginary lateral component of the wave vector), where an exponential decay of the wave amplitude results [57]. We have computed the cut-off frequencies of $\lambda/2$ thickness extensional mode to be 221.1 and 228.2 MHz in the metalized (short-circuited) region and non-metalized region, respectively. Because of the energy trapping, the loss mechanism associated with the Lamb waves carrying acoustic energy away from the resonator is suppressed, giving rise to low losses and high Q values.

B. Influence of Top Electrode Shape

To investigate the effect of the top electrode shape on the resonator response, in general, full 3D simulations are required. Here, we consider the cases of square, circular, and irregular quadrilateral top electrodes (see also [58]). FEM is validated by comparing the simulated displacement profiles with those measured for SMR resonators with a laser interferometer [29]. The laser probe is described in detail in [59].

Each resonator model consists of a 400-nm thick molybdenum bottom electrode, a 2050-nm thick ZnO layer, and a 400-nm thick aluminum top electrode. The thickness of the ZnO layer is chosen such that the measured and simulated series resonance frequencies for the resonator with a square top electrode are equal. The top and bottom surfaces are stress free, and the edges of the plate are fixed. The distance from the electrode edge to the fixed plate edge for models with square and circular top electrodes is

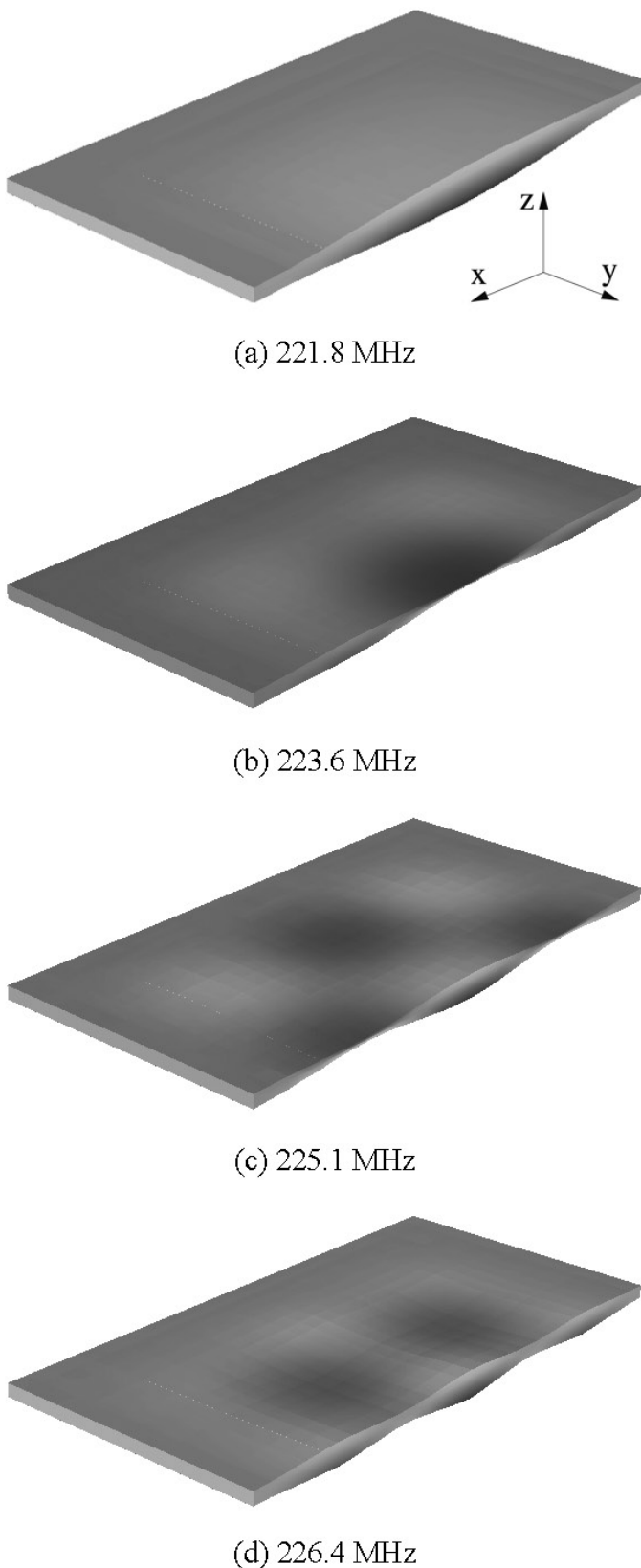


Fig. 12. Simulated displacement profiles at the selected resonances for the 3D model of the resonator. For clarity, only one-half of the resonator is shown; the other half is symmetric. The grayscale indicates the vertical (z) displacement. The displacements between different frequencies are not to scale.

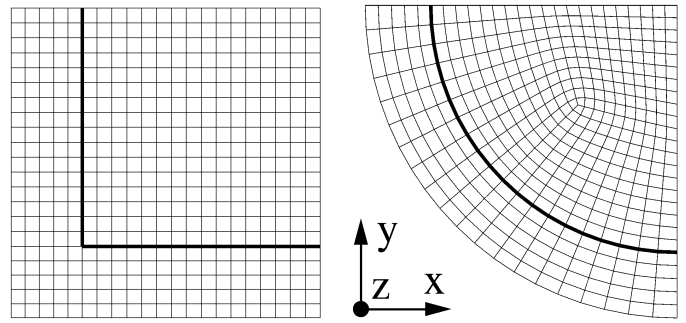


Fig. 13. Lateral element divisions of FEM meshes for the resonators with square and circular top electrodes. The meshes cover only one quadrant of the complete resonator. The edge of the electrode is indicated with the thick line.

30 μm . The area of the top electrode in all of the configurations is 40 000 μm^2 .

The number of elements in the thickness (z) direction in the molybdenum, the ZnO, and the aluminum layers is 1, 3, and 1, respectively. The lateral discretizations in FEM for the resonators with square and circular top electrodes are shown in Fig. 13.

1. Square Top Electrode. The model covers one quadrant of the actual resonator, and the symmetry BC are imposed: x - and y -components of the displacement vector vanish on the yz - and xz -symmetry planes, respectively. The simulated and measured displacement profiles on the top surface of the resonator with square top electrode are plotted for several frequencies in Fig. 14. In the computation of the displacements, the quality factor (Q) of 1500 is used for all modes [i.e., $Q_{sj} = 1500$ in (38)]. This value yields appropriate separation of the modes to match the measured mode shapes. In Fig. 14 through 17, the gray scale is such that the largest normalized magnitude of the z -displacement in each figure is indicated in white, and the lowest one is indicated in black. Similar displacement profiles for resonators with AlN as the piezoelectric and rectangular top electrode have also been measured by other authors and have been obtained with the atomic-force-microscope-based technique [60] and by laser interferometry [61], [62]. The ripple with a short spatial period observed in the simulated and measured displacement profiles is attributed to the standing wave pattern of high order anharmonic thickness shear modes. The fundamental frequency of these modes is below the operational frequency of the resonator considered here. However, the resolution of the computational mesh in Fig. 14 is not adequate to accurately model waves of such short wavelengths.

2. Circular Top Electrode. The case of a circular top electrode is simulated both with quadratic 3D and 2D axisymmetric elements. The measured and simulated magnitudes of the z -displacements obtained with 3D elements and 2D axisymmetric elements are illustrated in Fig. 15. Here, a Q -factor of 1000 is used for all modes. The measured frequencies are somewhat lower than those simulated, because, most probably, the ZnO layer in the mea-

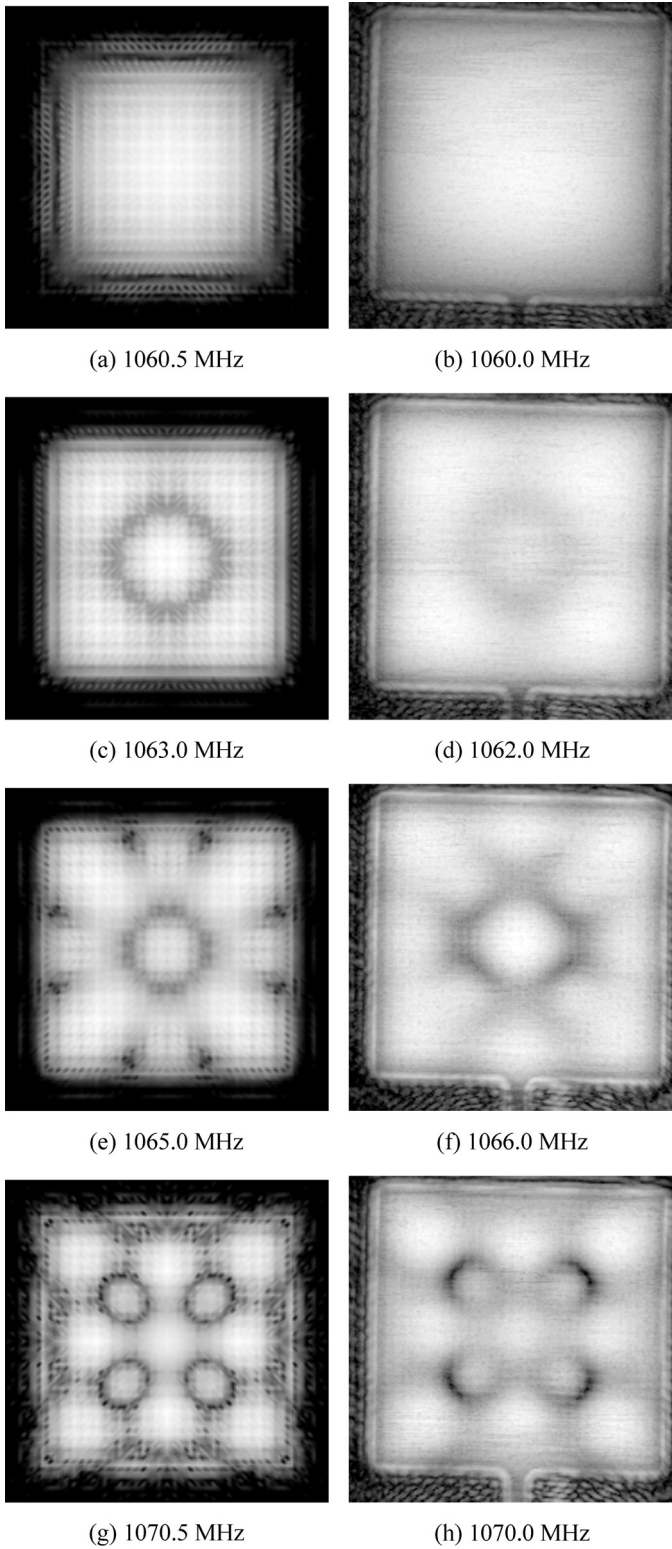


Fig. 14. Simulated (left) and measured (right) magnitudes of the z -displacements for the resonator with a square top electrode.

sured resonator with circular top electrode is thicker than that in the resonator with square top electrode.

3. Quadrilateral Top Electrode with No Parallel Sides:

It is suggested in [63], that irregular top electrode shapes could decrease the strength of the spurious modes. To test for this, the electrical response of a resonator featuring quadrilateral top electrode with no parallel sides has been simulated. The lateral element division in the FEM mesh is shown in Fig. 16. The simulated magnitudes of the displacement components in the z -direction on the top surface of the resonator as functions of frequency are plotted in Fig. 17. It is seen in Fig. 17(c, d, and e), that the mode with three displacement amplitude maxima across the electrode in the y -direction occurs first at the right-hand end of the electrode. As the frequency increases and the wavelength decreases, this amplitude profile moves toward the left, where the shorter electrode dimension in the y -direction is capable of supporting the mode. In Fig. 17(a, b, and f), regular displacement profiles are seen with 1×1 , 2×1 , and 4×2 vibration amplitude maxima in the x - and y -directions, respectively, with the number in the x -direction given first.

The static capacitances computed with FEM are 1.770 pF for the square; 1.764 pF and 1.755 pF for the circular top electrode configuration obtained with 3D elements and 2D axisymmetric elements, respectively; and 1.797 pF for the quadrilateral top electrode shape with no parallel sides. Fig. 18 shows the simulated frequency responses for the three top electrode geometries. Strong side resonances caused by anharmonic thickness extensional modes are observed at frequencies above the fundamental thickness extensional mode (approximately at 1060 MHz). Comparing the response of the irregular top electrode with those simulated for the square and circular top electrodes, it can be seen that, for the irregular top electrode, the onset of the strong side resonances occurs at a higher frequency, and the frequency spacing of the side resonances is larger. However, the response still shows spurious resonances with strengths approximately equal to those present in the responses simulated for square and circular top electrode shapes. Furthermore, the series resonance Q -factor in the case of the irregular top electrode can be seen to be slightly lower than in the cases of rectangular and circular top electrodes. Using 3D FEM, the shape of the top electrode can be easily varied to adjust the electrical response and to find a shape that minimizes the detrimental effects of the side resonances.

The discrepancies between the simulated and measured displacement profiles can be attributed mainly to the following effects.

- Fabrication inaccuracies, e.g., the actual resonator possesses a non-uniform piezoelectric layer thickness profile, whereas, in the FEM, all of the material layers have an ideal constant thickness. In addition, the material parameters are not accurately known.
- The simulated structure is a membrane-type resonator, rigidly supported at the plate edges, whereas

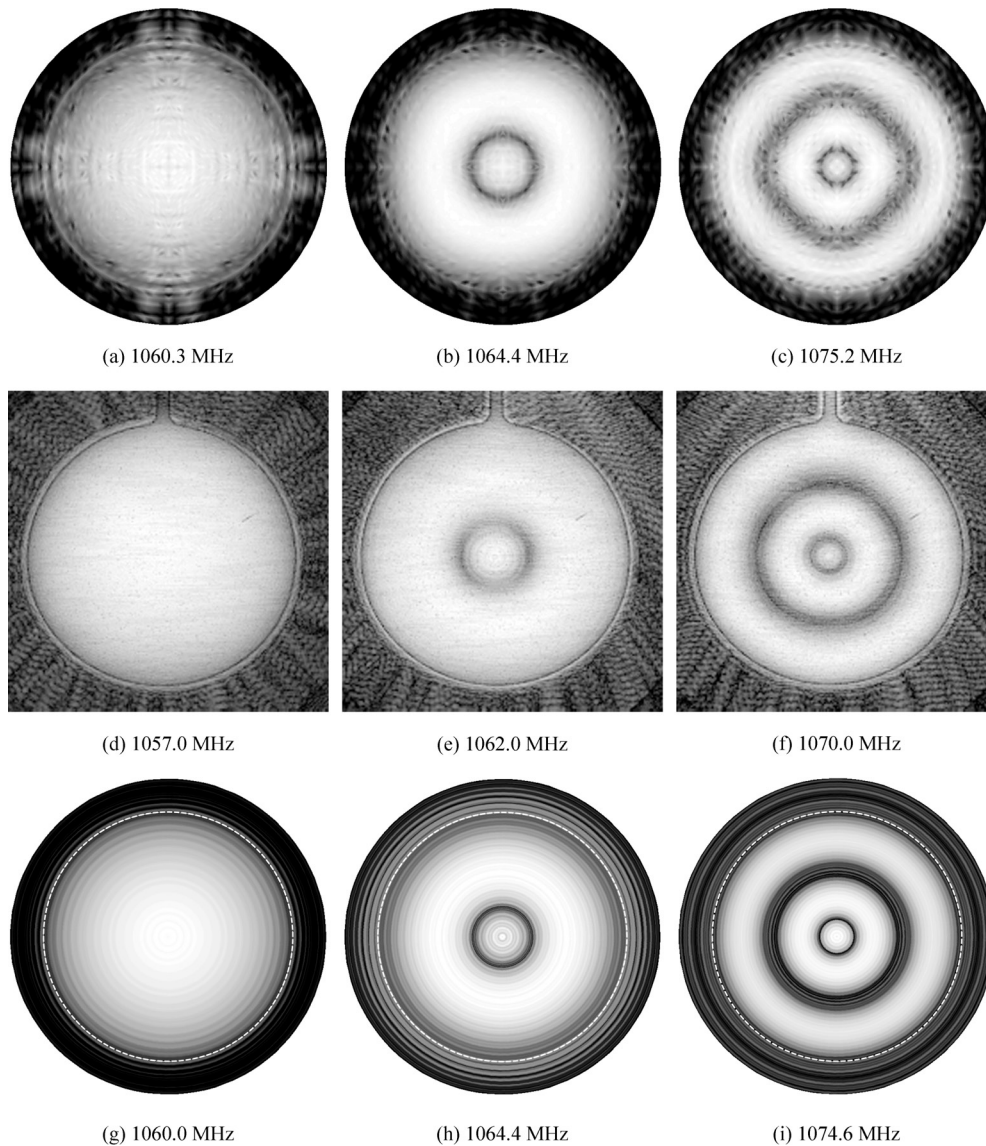


Fig. 15. Measured (middle row) and simulated magnitudes of displacement components in the z -direction for the resonator with a circular top electrode. In the 3D simulations (top row) and 2D simulations (bottom row), 20-node brick elements and 8-node quadrilateral axisymmetric elements are used, respectively. For the axisymmetric case, the top electrode edge is indicated with the white dashed line.

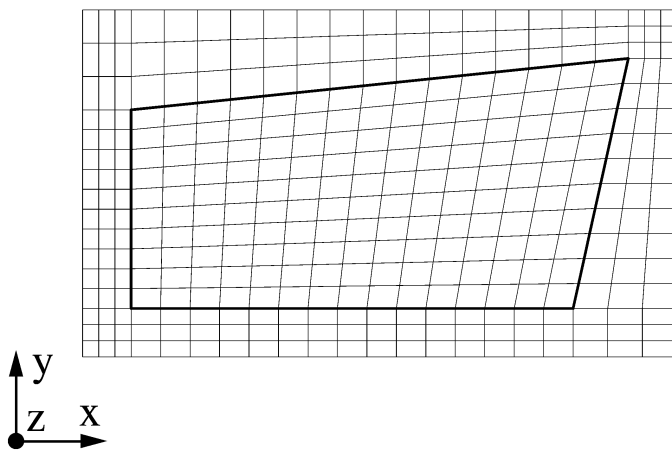


Fig. 16. Lateral element divisions of the FEM mesh for the resonator with asymmetric top electrode. The edge of the top electrode is indicated with the thick line.

the actual resonator is an SMR configuration. Adding the acoustic mirror layers below the resonator would significantly increase the computational cost in the 3D case.

- The Q -factors of the modes in the measurements and simulations are unequal, resulting in different overlaps of the modes.
- A comparatively coarse lateral discretization is used in the 3D FEM models.

Although the aspect ratios for the 3D elements used were rather large (15.6, 31.3, and 59.2 for the square, circular, and irregular quadrilateral cases, respectively), the accuracy in the resonance frequencies of the anharmonic thickness extensional modes above the main resonance frequency is reasonable. This is seen by comparing the admittances computed for the circular top electrode configuration using both the 3D and axisymmetric elements.

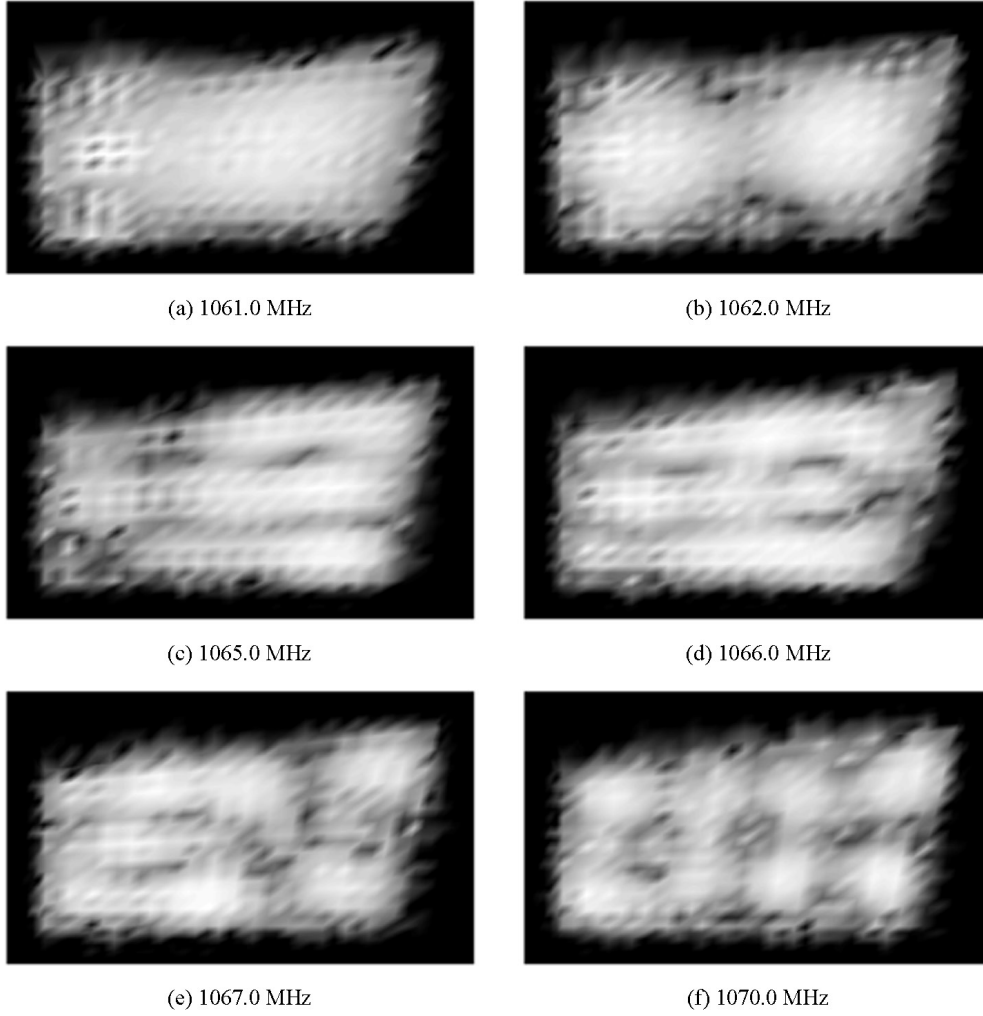


Fig. 17. Simulated magnitudes of displacement components in the z -direction as functions of frequency for the membrane resonator featuring quadrilateral top electrode with no parallel sides. In the computation of the displacements, a Q -factor of 1000 is used for all of the modes.

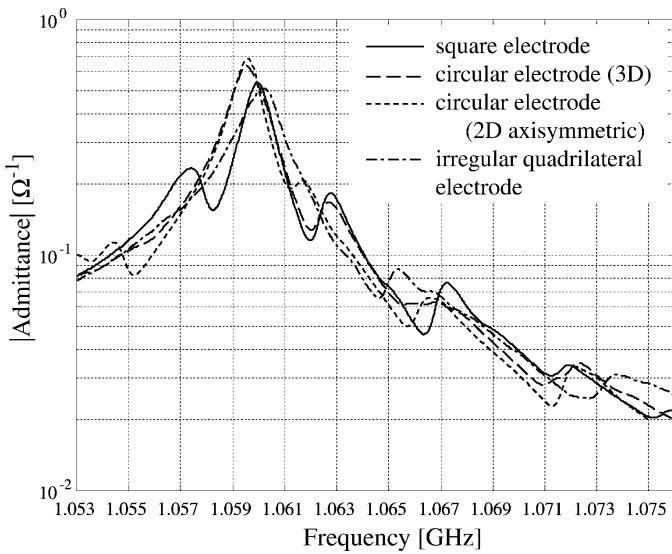


Fig. 18. Simulated admittances for resonators with various top electrode shapes obtained using FEM modal analysis (a Q -factor of 1000 has been used for all of the modes).

The computational parameters for the FEM simulations are displayed in Table I. The simulations were carried out with an SGI Origin 2000 computer. The execution times in Table I are only indicative, because they also depend on the total computational load in the multiuser environment. The effect of increasing the model size on the computing time in modal analysis is twofold. First, the execution time for solving each eigenpair increases. Second, the number of modes within a given frequency range of interest increases. For example, the 40 eigenpairs solved for model 5 in Table I spanned a bandwidth of 5.5 MHz.

VII. CONCLUSIONS

The FEM formulation for linear forced vibrations of piezoelectric media has been described. The harmonic analysis and modal analysis approaches to simulate the frequency characteristics of BAW resonators have been considered.

For the efficiency of the FEM modeling technique, the memory management method chosen and algorithms for

TABLE I
COMPUTATIONAL PARAMETERS FOR THE RESONATORS MODELED. THE MATRIX SIZES ARE IN MEGABYTES (MB).

Model ¹	Elements	Nodes	DOFs	Matrix half-bandwidth	Size of mass matrix	Size of stiffness matrix	Number of eigenpairs	CPU time(s)
1	1170	3737	9686	180	1.63	5.45	50	62.6
2	1400	7481	20 748	236	3.98	15.4	40	157.2
3	884	4587	14 371	2148	25.9	94.5	60	1289.9
4	1900	9391	30 642	2460	77.1	272	50	3006.6
5	2020	10 098	32 658	3048	85.6	322	40	4587.8
6	1494	7588	23 526	2540	46.3	173	40	2334.0

¹1 = Circular top electrode, 2D axisymmetric; 2 = 2D model of resonator in Fig. 9; 3 = 3D model of resonator in Fig. 9; 4 = circular top electrode, 3D; 5 = square top electrode, 3D; 6 = irregular quadrilateral top electrode, 3D.

solving the linear system of equations (in the harmonic analysis) and generalized eigenvalue problem (in the modal analysis) are of fundamental importance. The skyline storage scheme exploiting the characteristic structure of the mass matrix is employed in the interest of efficient memory usage. Consequently, simulations with more refined meshes for higher accuracy or simulations with larger models are possible. The application of cubic elements in 2D simulations provides an improved accuracy of the solution with less computational load in comparison with lower degree elements.

In the modal analysis, the Lanczos eigensolver is utilized in the computation of the natural resonance frequencies and the corresponding mode shapes within a specified bandwidth. Its efficiency results from the preservation of the sparse structure for the piezoelectric stiffness matrix. Furthermore, the modal constants quantifying the excitation strength for each resonant mode are computed. Subsequently, the approximate electrical admittance response can be computed in terms of the modal constants.

The FEM is applied to a thin-film membrane BAW resonators. The phenomenon of energy trapping is demonstrated, and the origin of the spurious modes in the anharmonic thickness extensional modes is emphasized. Comparison of results from 2D and 3D FEM simulations shows that, for most geometries, accurate analysis of resonator response requires full 3D modeling. The electrical response (admittance) and the displacements for resonators with various top electrode shapes are simulated. For square and circular top electrodes, the simulations are validated against laser interferometric measurements; the simulated magnitudes of the displacement components in the thickness (z) direction are found to agree well with the measurements. This shows that, although accurate 3D FEM simulations of composite BAW resonators would require a dense FEM mesh, rendering the simulations computationally intensive, valuable qualitative information on the performance of the resonator can be obtained from simulations requiring only moderate storage space and computing time. This is particularly true for the anharmonic thickness extensional modes with relatively long spatial wavelength in the vicinity of the fundamental thickness extensional mode.

The FEM simulations serve to analyze proposed resonator configurations and enable their comparison with respect to electrical performance. The dependence of the undesired parasitic resonances on the device structure, design, and dimensions can be investigated to help in the resonator design. Effects of manufacturing inaccuracies on the resonator response can also be studied. Moreover, the predictions of models based on approximate equations [37], [52], [64] can be tested and validated against 3D FEM.

ACKNOWLEDGMENTS

The authors thank J. Kaitila (VTT, Technical Research Centre of Finland) and P. Tikka (NMP) for manufacturing and measuring the resonator samples. The authors are also indebted to Dr. M. Ylilammi (VTT), I. Suni (VTT), and H. Pohjonen (NMP) for their valuable advice and inspiring discussions. Dr. Hermann Landes is acknowledged for providing the solver and matrix factorization algorithms for matrices in skyline format. The Center for Scientific Computing (CSC) is gratefully acknowledged for providing the computational resources.

REFERENCES

- [1] D. S. Burnett, *Finite Element Analysis*. Reading: Addison-Wesley, 1988.
- [2] K.-J. Bathe, *Finite Element Procedures*. Englewood Cliffs, NJ: Prentice Hall, 1996.
- [3] O. C. Zienkiewicz and R. L. Taylor, *The Finite Element Method*, vol. 1, 4th ed. London: McGraw-Hill, 1989.
- [4] H. Allik and T.J.R. Hughes, "Finite element method for piezoelectric vibration," *Int. J. Numer. Methods Eng.*, vol. 2, no. 2, pp. 151–157, 1970.
- [5] D. Boucher, M. Lagier, and C. Maerfeld, "Computation of the vibrational modes for piezoelectric array transducers using a mixed finite element-perturbation method," *IEEE Trans. Sonics Ultrason.*, vol. SU-28, no. 5, pp. 318–330, 1981.
- [6] G. L. Wojcik, D. K. Vaughan, N. Abboud, and J. Mould, Jr., "Electromechanical modeling using explicit time-domain finite elements," in *Proc. IEEE Ultrason. Symp.*, pp. 1107–1112, 1993.
- [7] M. Koshiba, S. Mitobe, and M. Suzuki, "Finite-element solution of periodic waveguides for acoustic waves," *IEEE Trans. Ultrason., Ferroelect., Freq. Contr.*, vol. 34, no. 4, pp. 472–477, 1987.

- [8] M. Buchner, W. Ruile, A. Dietz, and R. Dill, "FEM analysis of the reflection coefficient of SAWs in an infinite periodic array," in *Proc. IEEE Ultrason. Symp.*, pp. 371–375, 1991.
- [9] W. Friedrich, R. Lerch, K. Prestele, and R. Soldner, "Simulations of piezoelectric Lamb wave delay lines using a finite element method," *IEEE Trans. Ultrason., Ferroelect., Freq. Contr.*, vol. 37, no. 2, pp. 248–254, 1990.
- [10] J. T. Stewart and D. S. Stevens, "Three dimensional finite element modeling of quartz crystal strip resonators," in *Proc. IEEE Int. Freq. Contr. Symp.*, pp. 643–649, 1997.
- [11] H. Satoh, H. Suzuki, C. Takahashi, C. Narahara, and Y. Ebata, "A 400 MHz one-chip oscillator using and air-gap type thin film resonator," in *Proc. IEEE Ultrason. Symp.*, pp. 363–368, 1987.
- [12] W. A. Burkland, A. R. Landin, G. R. Kline, and R. S. Ketcham, "A thin-film bulk-acoustic-wave resonator-controlled oscillator on silicon," *IEEE Electron. Device Lett.*, vol. EDL-8, no. 11, pp. 531–533, 1987.
- [13] R. B. Stokes, J. D. Crawford, and D. Cushman, "Monolithic bulk acoustic filters to X-band in GaAs," in *Proc. IEEE Ultrason. Symp.*, pp. 547–551, 1993.
- [14] T. W. Grudkowski, J. F. Black, T. M. Reeder, D. E. Cullen, and R. A. Wagner, "Fundamental-mode VHF/UHF miniature acoustic resonators and filters on silicon," *Appl. Phys. Lett.*, vol. 37, no. 11, pp. 993–995, 1980.
- [15] K. M. Lakin and J. S. Wang, "Acoustic bulk wave composite resonators," *Appl. Phys. Lett.*, vol. 38, no. 3, pp. 125–127, 1981.
- [16] G. R. Kline and K. M. Lakin, "Composite thin film UHF bulk acoustic wave resonators on GaAs," in *Proc. IEEE Ultrason. Symp.*, pp. 495–497, 1983.
- [17] K. M. Lakin, G. R. Kline, and K. T. McCarron, "Development of miniature filters for wireless applications," *IEEE Trans. Microwave Theory Tech.*, vol. 43, no. 12, pp. 2933–2939, 1995.
- [18] H. Satoh, Y. Ebata, H. Suzuki, and C. Narahara, "An air-gap type piezoelectric composite thin film resonator," in *Proc. IEEE Int. Freq. Contr. Symp.*, pp. 361–366, 1985.
- [19] K. M. Lakin, G. R. Kline, and K. T. McCarron, "High-Q microwave acoustic resonators and filters," *IEEE Trans. Microwave Theory Tech.*, vol. 41, no. 12, pp. 2139–2146, 1993.
- [20] K. M. Lakin, "Modeling of thin film resonators and filters," *IEEE MTT-S Digest*, vol. 1, pp. 149–152, 1992.
- [21] K. M. Lakin, "Fundamental properties of thin film resonators," in *Proc. IEEE Int. Freq. Contr. Symp.*, pp. 201–206, 1991.
- [22] R. F. Milsom, D. T. Elliot, S. Terry-Wood, and M. Redwood, "Analysis and design of coupled-mode miniature bar resonators and monolithic filters," *IEEE Trans. Sonics Ultrason.*, vol. 30, no. 3, pp. 140–155, 1983.
- [23] R. F. Milsom, "Two-dimensional theory of thin-film ZnO resonators on silicon," in *Proc. IEEE Ultrason. Symp.*, pp. 484–489, 1982.
- [24] K. M. Lakin, "Analysis of composite resonator geometries," in *Proc. IEEE Int. Freq. Contr. Symp.*, pp. 320–324, 1983.
- [25] K. M. Lakin, "Numerical analysis of two dimensional thin film resonators," in *Proc. IEEE Int. Freq. Contr. Symp.*, pp. 502–508, 1993.
- [26] T. Shiosaki, T. Fukuichi, M. Tokuda, and A. Kawabata, "Temperature compensated high coupling and high quality factor ZnO/SiO₂ bulk wave resonators on high resistance substrates," in *Proc. IEEE Ultrason. Symp.*, pp. 405–410, 1984.
- [27] T. Makkonen, A. Holappa, and M. M. Salomaa, "Improvements in 2D FEM modeling software for crystal resonators," in *Proc. IEEE Ultrason. Symp.*, pp. 935–938, 1998.
- [28] K. M. Lakin, G. R. Kline, R. S. Ketcham, A. R. Landin, W. A. Burkland, K. T. McCarron, S. D. Braymen, and S. G. Burns, "Thin film resonator technology," in *Proc. IEEE Int. Freq. Contr. Symp.*, pp. 371–381, 1987.
- [29] P. T. Tikka, J. Kaitila, J. Ellä, T. Makkonen, J. V. Knuuttila, J. Westerholm, and M. M. Salomaa, "Laser probing and FEM modeling of solidly mounted resonators," in *Proc. IEEE MTT-S Int. Microwave Symp.*, pp. 1373–1376, 1999.
- [30] M. Naillon, R. H. Coursant, and F. Besnier, "Analysis of piezoelectric structures by a finite element method," *Acta Electronica*, vol. 25, no. 4, pp. 341–362, 1983.
- [31] J. Kocbach, P. Lunde, and M. Vestrheim, "FEMP-finite element modeling of piezoelectric structures theory and verification for piezoceramic disks," Department of Physics, University of Bergen, N-5007 Bergen, Norway, Sci. Tech. Rep. 1999-07, 1999.
- [32] J. F. Rosenbaum, *Bulk Acoustic Wave Theory and Devices*. Boston, MA: Artech House, 1988.
- [33] T. Ikeda, *Fundamentals of Piezoelectricity*. Oxford: Oxford University Press, 1996.
- [34] H. F. Tiersten, "Hamilton's principle for linear piezoelectric media," in *Proc. IEEE*, vol. 55, no. 8, pp. 1523–1524, 1967.
- [35] P.C.Y. Lee, "A variational principle for the equations of piezo-electromagnetism in elastic dielectric crystals," *J. Appl. Phys.*, vol. 69, no. 11, pp. 7470–7473, 1991.
- [36] R. D. Mindlin, "High frequency vibrations of piezoelectric crystal plates," *Int. J. Solids Structures*, vol. 8, no. 7, pp. 895–906, 1972.
- [37] P.C.Y. Lee, S. Syngellakis, and J. P. Hou, "A two-dimensional theory for high-frequency vibrations of piezoelectric crystal plates with or without electrodes," *J. Appl. Phys.*, vol. 61, no. 4, pp. 1249–1262, 1987.
- [38] R. Lerch, "Simulation of piezoelectric devices by two- and three-dimensional finite elements," *IEEE Trans. Ultrason., Ferroelect., Freq. Contr.*, vol. 37, no. 2, pp. 233–247, 1990.
- [39] B. A. Auld, *Acoustic Fields and Waves in Solids*, vol. 1, New York: John Wiley & Sons, 1973.
- [40] R. Holland, "Representation of dielectric, elastic, and piezoelectric losses by complex coefficients," *IEEE Trans. Sonics Ultrason.*, vol. SU-14, no. 1, pp. 18–20, 1967.
- [41] N. Saiga, K. Kajitani, and T. Suzuki, "Finite element simulation of local vibration of a piezoelectric plate considering energy losses," *Jpn. J. Appl. Phys.*, vol. 22, Supplement 22-3, pp. 33–35, 1983.
- [42] E. E. Antonova and P. P. Silvester, "Finite elements for piezoelectric vibrations with open electric boundaries," *IEEE Trans. Ultrason., Ferroelect., Freq. Contr.*, vol. 44, no. 3, pp. 548–556, 1997.
- [43] M. Gindre, W. Urbach, R. H. Coursant, and M. Fink, "Mechanical displacement induced in a piezoelectric structure: Experimental measurement by laser interferometry and simulation by a finite element method," *J. Acoust. Soc. Amer.*, vol. 84, no. 1, pp. 11–19, 1988.
- [44] H. Allik, K. M. Webman, and J. T. Hunt, "Vibrational response of sonar transducers using piezoelectric finite elements," *J. Acoust. Soc. Amer.*, vol. 56, no. 6, pp. 1782–1791, 1974.
- [45] N. Guo, P. Cawley, and D. Hitchings, "The finite element analysis of the vibration characteristics of piezoelectric discs," *J. Sound Vibration*, vol. 159, no. 1, pp. 115–138, 1992.
- [46] N. Guo and P. Cawley, "Measurement and prediction of the frequency spectrum of piezoelectric disks by modal analysis," *J. Acoust. Soc. Amer.*, vol. 92, no. 6, pp. 3379–3388, 1992.
- [47] Dept. of Computational and Applied Mathematics, Rice University, TX. (1996). ARPACK software. [Online]. Available: <http://www.caam.rice.edu/software/ARPACK>.
- [48] Y.-K. Yong and Y. Cho, "Algorithms for eigenvalue problems in piezoelectric finite element analyses," in *Proc. IEEE Ultrason. Symp.*, pp. 1057–1062, 1994.
- [49] J. G. Lewis, "Implementation of the Gibbs-Poole-Stockmeyer and Gibbs-King algorithms," *ACM Trans. on Mathematical Software*, vol. 8, no. 2, pp. 180–189, 1982.
- [50] Y.-K. Yong and Y. Cho, "Numerical algorithms for solutions of large eigenvalue problems in piezoelectric resonators," *Int. J. Numer. Methods Eng.*, vol. 39, no. 6, pp. 909–922, 1996.
- [51] Y.-K. Yong, J. T. Stewart, and A. Ballato, "A laminated plate theory for high frequency, piezoelectric thin-film resonators," *J. Appl. Phys.*, vol. 74, no. 5, pp. 3028–3046, 1993.
- [52] Z. Zhang and Y.-K. Yong, "Numerical analysis of thickness shear thin film piezoelectric resonators using a laminated plate theory," *IEEE Trans. Ultrason., Ferroelect., Freq. Contr.*, vol. 42, no. 4, pp. 734–746, 1995.
- [53] R. F. Milsom, J. E. Curran, S. L. Murray, S. Terry-Wood, and M. Redwood, "Effect of mesa-shaping on spurious modes in ZnO/Si bulk-wave composite resonators," in *Proc. IEEE Ultrason. Symp.*, pp. 498–503, 1983.
- [54] P. Bettess, *Infinite Elements*. Sunderland: Penshaw Press, 1992.
- [55] D. S. Burnett, "A three-dimensional acoustic infinite element based on a prolate spheroidal multipole expansion," *J. Acoust. Soc. Amer.*, vol. 96, no. 5, pp. 2798–2816, 1994.
- [56] K. M. Lakin, G. R. Kline, and K. T. McCarron, "Thin film bulk acoustic wave filters for GPS," in *Proc. IEEE Ultrason. Symp.*, pp. 471–476, 1992.

- [57] W. Shockley, D. R. Curran, and D. J. Koneval, "Energy trapping and related studies of multiple electrode filter crystals," in *Proc. IEEE Int. Freq. Contr. Symp.*, pp. 88–126, 1963.
- [58] T. Makkonen, A. Holappa, and M. M. Salomaa, "3D FEM modeling of composite BAW resonators," in *Proc. IEEE Ultrason. Symp.*, pp. 893–896, 2000.
- [59] J. V. Knuuttila, P. T. Tikka, and M. M. Salomaa, "Scanning Michelson interferometer for imaging surface acoustic wave fields," *Optics Lett.*, vol. 25, no. 9, pp. 613–615, 2000.
- [60] H. Safar, R. N. Kleiman, B. P. Barber, P. L. Gammel, J. Pastalan, H. Huggins, L. Fetter, and R. Miller, "Imaging of acoustic fields in bulk acoustic-wave thin-film resonators," *Appl. Phys. Lett.*, vol. 77, no. 1, pp. 136–138, 2000.
- [61] J. E. Graebner, "Optical scanning interferometer for dynamic imaging of high-frequency surface motion," in *Proc. IEEE Ultrason. Symp.*, pp. 733–736, 2000.
- [62] J. E. Graebner, H. F. Safar, B. Barber, P. L. Gammel, J. Herbsommer, L. A. Fetter, J. Pastalan, H. A. Huggins, and R. E. Miller, "Optical mapping of surface vibrations on a thin-film resonator near 2 GHz," in *Proc. IEEE Ultrason. Symp.*, pp. 635–638, 2000.
- [63] J. D. Larson, III, R. C. Ruby, and P. Bradley, "Bulk acoustic wave resonator with improved lateral mode suppression," Eur. Patent EP 1041717A2, Oct. 4, 2000.
- [64] R. C. Peach, "A variational method for the design of trapped energy resonators," in *Proc. IEEE Int. Freq. Contr. Symp.*, pp. 392–399, 1985.



Tapani Makkonen (M'98) was born in Helsinki, Finland in 1968. He received the MSc degree in engineering physics from the Helsinki University of Technology in June 1996, after which he joined the Materials Physics Laboratory as a PhD student. His research interests include BAW and SAW physics, FEM of BAW devices, and the modeling of package parasitic effects. Mr. Makkonen is a member of the Finnish Physical Society.



Antti Holappa was born in Imatra, Finland in 1974. He is a MSc student in engineering physics at the Helsinki University of Technology. He has been working as a technology specialist in Smartner Information Systems Ltd. since October 2000.



Juha Ellä was born in Helsinki, Finland in 1967. He received his MSc degree in electrical engineering from the Helsinki University of Technology in June 1994, after which he joined Nokia Mobile Phones Ltd. His research interests include RF-integration and filtering in the field of cellular applications and, particularly, the design and modeling of BAW devices and their packages.



Martti M. Salomaa received his DrTech degree in technical physics from Helsinki University of Technology (HUT) in 1979. Thereafter, he worked at UCLA and the University of Virginia. From 1982 to 1991, he was the theory group leader at the Low Temperature Laboratory, HUT, and from 1988 to 1991, he served as Director of the ROTA project between the Academy of Finland and the Soviet Academy of Sciences. He has held a sabbatical stipend at the University of Karlsruhe, and, in 1994, he was Guest Professor at ETH-Zürich. Since 1994, he has been an associate professor and, since 1996, a full professor in technical physics and the Director of the Materials Physics Laboratory in the Department of Engineering Physics and Mathematics at HUT. He is a co-recipient of the 1987 Award for the Advancement of European Science (presented by the Körber Foundation, Hamburg). His research interests include superfluidity, superconductivity, magnetism, physics of SAW, nondiffracting waves, and mesoscopic physics. He is a member of the IEEE, APS, EPS, and the Finnish Physical and Optical Societies.